High Mass Star Formation II: The Mass Function of Submillimeter Clumps in M17

Michael A. Reid and Christine D. Wilson

Department of Physics and Astronomy, McMaster University, Hamilton, ON, L8S 4M1, Canada
& Harvard-Smithsonian Submillimeter Array Project, 645 N A'ohoku Pl., Hilo, HI, 96720, USA

ABSTRACT

We have mapped a $\sim 5.5 \times 5.5$ pc portion of the M17 massive star-forming region in both 850 and 450 μm dust continuum emission using the Submillimeter Common-User Bolometer Array (SCUBA) on the James Clerk Maxwell Telescope (JCMT). The maps reveal more than 100 dusty clumps with deconvolved linear sizes of $\sim$0.05–0.2 pc and masses of $\sim$0.8–120 $M_\odot$, most of which are not associated with known mid-infrared point sources. Fitting the clump mass function with a double power law gives a mean power law exponent of $\alpha_{\mathrm{high}} = -2.4 \pm 0.3$ for the high-mass power law, consistent with the exponent of the Salpeter stellar mass function. We show that a lognormal clump mass distribution with a peak at $\sim$4 $M_\odot$ produces as good a fit to the clump mass function as does a double power law. This 4 $M_\odot$ peak mass is well above the peak masses of both the stellar initial mass function and the mass function of clumps in low-mass star-forming regions. Despite the difference in intrinsic mass scale, the *shape* of the M17 clump mass function appears to be consistent with the shape of the core mass function in low-mass star-forming regions. Thus, we suggest that the clump mass function in high-mass star-forming regions may be a scaled-up version of that in low-mass regions, instead of its extension to higher masses.

Subject headings: stars: formation — ISM: individual (M17) — submillimeter — ISM: structure — methods: data analysis

1.   INTRODUCTION

Numerous unresolved aspects of the theory of star formation depend on a detailed knowledge of the structure of the interstellar medium in star-forming regions. For example, it is well established that the turbulent fragmentation of molecular clouds gives rise to a variety of small-scale structures, some of which collapse gravitationally to form stars (e.g., Testi & Sargent 1998; Motte et al. 2001; Klessen 2001; Klessen & Burkert 2000). However, it is not clear what determines the final, relatively invariant distribution of stellar masses. In order to identify the processes which set the stellar mass function, we must first know how the masses of pre-stellar cores and clumps are distributed.

Submillimeter continuum observations of low-mass star-forming regions have suggested that the mass function of 10^3–10^4 AU-scale dense clumps with masses less than a few $M_\odot$ resembles the stellar initial mass function (IMF) over the same mass range (Testi & Sargent 1998; Johnstone et al. 2000; Motte et al. 2001). It is less clear how the mass function of massive clumps/cores relates to that of massive stars, mostly due to a lack of submillimeter continuum observations of massive star-forming regions at sufficiently high resolution. The relationship between the masses of cores and stars is especially important at higher masses because it could help to distinguish between competing theories of high-mass star-formation. According to the two prevailing theories, massive stars may form either by the monolithic collapse of individual molecular cloud cores (McKee & Tan 2002, 2003; Krumholz 2005), aided by the formation of a disk and an optically thin outflow cavity, or by the competitive accretion of material from the larger reservoir of an entire proto-cluster (Bonnell et al. 1997, 2001a,b; Bonnell & Bate 2002). In principle, we should expect a closer resemblance between the mass functions of cores and stars in the first case than in the second. Whatever the formation mechanism of massive stars, it is likely to have signature in the clump/core mass function.

To date, only a handful of studies have measured the submillimeter continuum mass function of cores and clumps at and beyond the high-mass end of the stellar mass range (Kerton et al. 2001; Tothill et al. 2002; Motte et al. 2003; Reid & Wilson 2005, "Paper I" hereafter). Because the mean distance to massive star-forming regions is large compared to their low-mass counterparts, most studies of such regions have been sensitive only to spatial and mass scales significantly larger than those of pre-stellar clumps (Motte et al. 2003; Mookerjea et al. 2004). In this paper and Paper I, we present submillimeter continuum maps of two relatively nearby massive star-forming regions, in which it is possible to discern structures which may form individual stars. Paper I concentrated on NGC 7538, a massive star-forming region at a distance of 2.8 kpc. The focus of this paper is M17 which, at a distance of 1.6 ± 0.3 kpc (Nielbock et al. 2001), is near enough to permit us to discern candidate pre-stellar condensations. The $\sim 8''$ beam of the James Clerk Maxwell Telescope at 450 μm translates to a linear resolution of ~ 0.06 pc ($\sim 1.3 \times 10^4$ AU) at 1.6 kpc, which is comparable to the resolution obtained in similar observations of nearby low-mass star-forming regions (typically 0.01–0.03 pc).

A large-scale CO J=1$\rightarrow$0 map of M17 shows it to be divided into northern and southern parts whose combined mass exceeds $3 \times 10^4 M_\odot$ (Lada 1976). The best-known features of the region are the well-studied photon-dominated region and the molecular cloud it borders, M17SW (e.g., Brogan & Troland 2001; Stutzki & Güsten 1990; Felli et al. 1984). M17SW exhibits many signs of massive star formation, including an ultracompact HII (UCHII) region, numerous locations of maser activity, and a cluster of young O and B type stars (Hanson et al. 1997; Chini et al. 2000; Brogan & Troland 2001). In their survey of 69 stars in M17, Chini & Wargau (1998) found 20 stars with strong infrared excesses and luminosities more than 60 times those of Class I sources in ρ Oph. They identify these sources as candidate massive Class I analogs, which suggests that there is a significant population of young, early type massive stars in the region.

Because we are interested in studying the earliest stages of massive star formation, rather

than study M17SW, where massive star formation is already well underway, we focus instead on the northern part of M17, in the region around the compact source M17N. The CO maps of Lada (1976) and Wilson et al. (1999) show the M17N region to be rich in molecular gas, but radio continuum studies (e.g., Lada et al. 1976) show it to be relatively devoid of free-free emission, which suggests it is relatively free of ionizing massive stars. Most of the detected radio continuum emission originates in the UCHII region associated with M17N (Wilson et al. 1979), which coincides with an H_2O maser (Jaffe et al. 1981). At least 5 infrared point sources in the immediate vicinity of M17N are believed to be embedded stars (Klein et al. 1999; Henning et al. 1998).

Klein et al. (1999) made a $3' \times 4'$ map of the region around M17N at 1.3 mm with the IRAM 30m telescope, which revealed the extended, clumpy nature of the dust continuum emission. In order to identify new cold, dusty clumps in the M17N region and to characterize their mass function, we have obtained larger, more sensitive maps of the region at 450 μm and 850 μm. In §2, we describe our observations and data reduction techniques. In §3, we discuss the properties of the clumps. Section 5 is devoted to a detailed analysis of the M17 clump mass function, including comparisons to the mass function of CO clumps and the stellar IMF. In Paper III, the results of Papers I and II will be compared quantitatively to the clump mass functions measured in other star-forming regions, with the goal of determining a general functional form for the clump mass function.

2.   OBSERVATIONS AND DATA REDUCTION

We used the Submillimeter Common-User Bolometer Array on the James Clerk Maxwell Telescope to map an approximately $12' \times 12'$ (5.5×5.5 pc) region of M17. The data were acquired on the nights of 2003 March 17 and April 16 with a total on-source integration time of about 5 hr. The data were taken in the standard scan-mapping mode with chop throws of $30''$, $44''$, and $68''$ in both right ascension and declination. Pointing checks were performed once per hour and sky dips once every hour or two. The rms pointing accuracy was approximately $1.7''$. Mars was used as the flux calibrator and was observed every 3–4 hours; the derived uncertainties in the gain calibrations were 4% at 450 μm and 12% at 850 μm. The sky opacities at 850 μm and 450 μm were calculated using polynomial fits to the combination of the JCMT skydips and the 225 GHz zenith optical depth measurements from the Caltech Submillimeter Observatory. The mean 225 GHz zenith optical depths on the two nights were 0.093 and 0.054, respectively. The mean residuals from the polynomial fits to the optical depth data translate into a systematic uncertainty in the fluxes of less than 1%.

We used the standard techniques for reducing and calibrating SCUBA scan maps (detailed in Paper I), including map reconstruction with the Emerson2 algorithm (Emerson 1995). The mean rms flux measured in emission-free regions of the maps is 0.027 Jy beam^{-1} at 850 μm and 0.32 Jy beam^{-1} at 450 μm. These rms fluxes are somewhat higher than those from Paper I (0.021 Jy beam^{-1} and 0.18 Jy beam^{-1} at 850 μm and 450 μm, respectively), but M17 is nearly twice as close as NGC 7538, making the M17 maps significantly more sensitive in terms of luminosity.

The half power beam widths at the two wavelengths were $15.4''$ and $8.5''$, respectively. We used the "image flattening" technique described in Paper I to remove spurious large-scale structure introduced during reconstruction of the scan map using the Emerson2 technique. The flattening technique consists of clipping the brightest emission peaks from the map, smoothing the remainder to approximate the large-scale background of the map, and subtracting the result from the original map. The technique preserves all structure on scales smaller than approximately twice the size of the largest chop throw, or about $2'$. Because the strongest source in the maps (M17N) is considerably weaker than the strongest source in the NGC 7538 region, the small artifacts introduced by the flattening technique are even smaller in the M17 maps than in the NGC 7538 maps. The only visible effect of the flattening procedure is a slight reduction in the brightness of the structure extending northward from M17N. The 850 μm and 450 μm maps are shown in Figures 1 and 2, respectively.

3. PROPERTIES OF THE M17 CLUMPS

3.1. Clump Identification and Contamination Corrections

We used *clfind2d* (Williams et al. 1994) to locate the clumps in our maps and determine their boundaries and integrated fluxes. To be considered a clump, an object must satisfy three criteria: its area must be at least half that of the beam, its peak flux must be at least 5 σ, and it must have a flux of $> 3\ \sigma$ in every pixel. Using *clfind2d* with these detectability criteria, we identified 121 clumps in the 850 μm image and 101 in the 450 μm image. The properties of the 850 μm and 450 μm clumps are listed in Tables 1 and 2, respectively. Note that the clump radii stated throughout this paper are the effective radii of the clumps, deconvolved from the beam. The effective radius of a clump is defined as the radius of a circle with an area equal to the projected area of the clump.

As we are principally interested in the dust continuum emission of each clump, we must correct the fluxes for three likely sources of contamination: radio continuum emission, CO J=3→2 line emission in the 850 μm filter, and the sometimes substantial JCMT error beam.

3.1.1. Radio Continuum Corrections to $S_{\rm int}$

Radio continuum contamination is principally a concern in M17N, which harbors an UCHII region (Wilson et al. 1979), and in the southeastern part of the map, where some of the dust continuum emission is coincident with the "Northern Bar" structure seen in numerous radio continuum studies (e.g., Brogan & Troland 2001; Felli et al. 1984). Combining the measured 1.4 and 3.5 cm radio continuum fluxes of M17N from Lada et al. (1976) and Wilson et al. (1979), respectively, with the assumption that the radio continuum emission follows a power law of the form $S_\nu \propto \nu^{-0.1}$, we estimate the radio continuum contamination of M17N at 850 μm to be $\sim$30%, or $\sim$2.2 Jy. We used

the 6 cm map of Felli et al. (1984) to estimate radio continuum corrections to the 850 μm fluxes of the 18 clumps which are coincident with the Northern Bar, again assuming the $S_\nu \propto \nu^{-0.1}$ scaling relationship. The corrections to the 850 μm fluxes derived in this way ranged from 4 to 45%, but were typically less than 20%. Radio continuum corrections to the 450 μm fluxes were found to be negligible. The remainder of the clumps in the map are not coincident with any known radio continuum sources (see, for example, the map of Lada et al. 1976).

3.1.2.   CO $J=3\rightarrow2$ Corrections to S_{int}

The derivation of CO $J=3\rightarrow2$ contamination corrections is complicated by the lack of a CO $J=3\rightarrow2$ map with the same spatial resolution and coverage as our continuum maps. The closest match is the CO $J=3\rightarrow2$ map of Wilson et al. (1999), which completely covers our map, but is not fully sampled. The Wilson et al. (1999) map was made using the position-switching technique instead of chopping. Thus, it traces the total column of CO $J=3\rightarrow2$, while our chopped maps can suffer contamination only from CO $J=3\rightarrow2$ emission on scales smaller than about twice our largest chop throw, or $\sim2'$. Comparing our maps to those of Wilson et al. (1999) reveals that most of the CO structure in the region of overlap occurs on large spatial scales, greater than $2'$. Hence, most of this emission would be chopped out in our map, and would not contaminate the 850 μm fluxes. We expect the CO contamination to be worst close to M17N, where the CO emission peaks. We estimate that the CO contamination of the 850 μm flux of the clump associated with M17N would be about 26% if we were sensitive to the total column of CO, but half or less than that in the chopped map. Because the degree of CO contamination is difficult to estimate, but likely less than 10% in most clumps, we have not applied CO corrections to our data.

3.1.3.   Error Beam Corrections to S_{int}

The JCMT beam can be reasonably approximated by a sum of Gaussian components: a strong, narrow primary beam and a broad, faint error beam. In Paper I, we described our method for fitting the beam structure using our calibrator observations. In this work, we used the same beam fits as in Paper I to correct the integrated flux of each clump. The error beam corrections at 850 μm ranged from 3 to 14% with a mean of 10%. The equivalent corrections at 450 μm ranged from 3 to 18% with a mean value of 11%.

3.2.   Clump Spectral Indices and Temperatures

We have used the combination of our 850 μm and 450 μm maps to measure the spectral index, α, of each clump, and thereby to estimate its temperature. The spectral index in a given pixel of the map is defined as:

$$\alpha = \frac{\log(S_{450\mu m}/S_{850\mu m})}{\log(850/450)} \quad . \tag{1}$$

As described in detail in Paper I, it is necessary first to match the beams of the two images by convolving each map with the beam at the other wavelength. This method not only ensures that the resolutions of the two maps match, but also that their error beam structures match. We applied the *clfind2d* boundaries of the 850 μm clumps to the spectral index map to calculate the flux-weighted mean spectral index of each 850 μm clump. In computing the flux-weighted mean spectral index, we weight the spectral index of each pixel by the flux of the corresponding pixel in the convolved (i.e. resolution-matched) 850 μm map. Only pixels detected at $> 3\sigma$ at both 850 μm and 450 μm are included in the mean. The mean spectral indices so calculated are given in Table 1. The $\sim 18''$ beam of the spectral index map prohibits direct comparison between it and the 450 μm map, whose beam is less than half as broad. The broader $\sim 15''$ beam of the 850 μm map permits direct comparisons with the spectral index map. Making this comparison, we find, as in Paper I, that continuum emission peaks in the 850 μm map are strongly correlated with peaks in the spectral index map.

We can use the derived spectral indices to estimate the mean temperature of each clump. The mean flux ratio of a clump is related to its mean dust temperature, $\langle T_{dust} \rangle$, and mean dust emissivity index, $\langle \beta \rangle$ by:

$$\left\langle \frac{S_{450\mu m}}{S_{850\mu m}} \right\rangle = \frac{e^{16.9/\langle T_{dust} \rangle} - 1}{e^{32.0/\langle T_{dust} \rangle} - 1} \left(\frac{850}{450} \right)^{3+\langle \beta \rangle} \quad , \tag{2}$$

where angle brackets denote spatial averages over each clump's area and the numerical exponents are the $h\nu/k$ terms from the Planck function. Although we expect β to vary somewhat with varying dust properties throughout massive star-forming regions, we presently have no means by which to quantify these variations. For simplicity, we assume a spatially invariant value of $\langle \beta \rangle = 1.5$, consistent with the results of Dupac et al. 2002, who derived $\beta = 1.6 \pm 0.2$ for M17N, and Sandell & Sievers 2004, who derived β values ranging from 1.2 to 2 for massive clumps in NGC 7538.

Using our assumed β value and the flux ratios derived from the spectral index map, we can use Equation 2 to compute the mean dust temperature of each clump. Again, due to the resolution mismatch between the 450 μm and spectral index maps, this technique can only be applied to the 850 μm clumps. Note that it is not possible to estimate temperatures for all of the 850 μm clumps. The spectral index map contains only those pixels detected at $> 3\sigma$ in both the 850 μm and 450 μm images, so no spectral index can be derived for the thirteen 850 μm clumps which are not strongly detected at 450 μm. An additional ten clumps have measured flux ratios which are larger than the high temperature asymptotic value of the flux ratio from Eq. 2. The presence of such high flux ratios probably reflects a breakdown in our assumption of a spatially invariant β, with unusually high flux ratios tracing regions of elevated β. The estimated temperatures of

the remaining 98 clumps are given in Table 1. They range from 6 to 235 K, with a mean value of 33 K and a median value of 20 K. We derive the random uncertainties on these temperatures from the uncertainties in the gains, sky opacities, and the error beam fits. The exponential form of Equation 2 dictates that the width of the temperature uncertainty interval increases rapidly with temperature and that the upper uncertainty interval quickly exceeds the lower. Typical random uncertainties on the estimated temperatures, which derive from the uncertainties in the gain and sky opacity calibrations, are ± 1.5 K below 10 K, ± 5 K between 10 and 20 K, $^{+10}_{-7}$ K between 20 and 30 K, $^{+20}_{-10}$ K between 30 and 40 K, and $^{+50}_{-15}$ K above 40 K.

Additional uncertainty enters via our choice of β: a clump with $T_d = 15$ K for $\beta = 1.5$ would have $T_d = 11$ K for $\beta = 2$ and $T_d = 21$ K for $\beta = 1.2$. The equivalent uncertainty range for a clump with $T_d = 30$ K would be ~ 16–90 K. For these reasons, all of the temperatures above ~ 30 K should be considered highly uncertain, indicating only that a core is probably "hot". Despite the uncertainties in their absolute values, the estimated temperatures still offer a means to rank the clumps by temperature. One possible exception would be cases where two clumps having different temperatures lie within the same JCMT beam; we cannot rule out such occurrences. To facilitate visualization of the distribution of clump temperatures, the clump symbols in Figure 1 are color-coded according to temperature.

3.3. Clump Masses

Assuming that the dust emission is optically thin, the integrated dust continuum flux of a clump can be converted to a total clump mass via:

$$M_{\text{clump}} = \frac{S_\lambda^{\text{int}} d^2}{\kappa_\lambda B_\lambda(T_{\text{dust}})} \quad , \tag{3}$$

where M_{clump} is the total gas and dust mass of the clump, S_λ^{int} is the flux at wavelength λ integrated over the clump boundary defined by *clfind2d*, d is the distance to the clump (taken to be 1.6 kpc), κ_λ is the dust opacity per unit mass column density at wavelength λ, and $B_\lambda(T_{\text{dust}})$ is the Planck function evaluated at temperature T_{dust}. Assuming, as previously, a spatially invariant $\beta = 1.5$, a gas-to-dust ratio of 100, and the Hildebrand (1983) prescription for the dust opacity, $\kappa_\lambda = 0.1(250\mu m/\lambda)^\beta$, we obtain $\kappa_{850\mu m} = 0.0087$ cm^2 g^{-1} and $\kappa_{450\mu m} = 0.031$ cm^2 g^{-1}. This is the same prescription used in Paper I to calculate the masses of the clumps in NGC 7538, and very closely mirrors those typically used in similar studies of the dusty clumps in low-mass star-forming regions (c.f. Johnstone et al. 2000, Motte et al. 2001).

We adopt two separate approaches to the remaining parameter in Eq. 3, the dust temperature. As a baseline approach, we make the simplifying assumption that all clumps are isothermal and characterized by a mean dust temperature of ~ 30 K. This is consistent with the dust temperature of 28 ± 3 K found by Dupac et al. (2002) using multi-wavelength PRONAOS dust continuum

observations of M17N. The masses calculated under this assumption range from 0.8 to 120 $M_\odot$ for the 850 μm clumps, and from 1.8 to 160 $M_\odot$ for the 450 μm clumps. The median clump masses at 850 μm and 450 μm are 12 and 13 $M_\odot$, respectively. The total mass of the clumps detected at 850 μm and 450 μm are 2900 and 2000 $M_\odot$, respectively. In the 98 cases where we were able to estimate the mean dust temperature of each 850 μm clump individually, we have used these temperatures to produce another estimate of their masses. The clump masses so calculated range from 0.3 to 200 $M_\odot$, with a median value of 32 $M_\odot$. Clump masses calculated in both of these ways are given in Tables 1 and 2. The masses calculated from the 850 μm fluxes are likely more accurate than those calculated from the 450 μm fluxes, as the latter suffer from lower signal-to-noise and larger error beam corrections.

Like the temperatures, the masses are also affected by the choice of β. A β value of 2.0 would give 850 μm and 450 μm masses which were 0.54 and 0.75 times the stated values, respectively. For $\beta = 1.2$, the 850 μm and 450 μm masses would be 1.4 and 1.2 times higher, respectively. Note, however, that a change in the assumed constant value of β does not change the shape of the clump mass function.

3.4.   Correlations With Signposts of Star Formation

To assess the likely evolutionary states of the clumps in our map, we searched for spatial correlations between clumps and tracers of massive star formation, such as outflows, masers, and compact infrared sources. The mapped region of M17 does not appear to have been surveyed for outflow sources. Jaffe et al. (1981) surveyed our entire mapped region for 22 GHz water masers, locating only one, which is coincident with M17N within the positional uncertainties (see Fig. 1). To check for the presence of infrared sources, we compared our dust continuum clumps with the point source catalog from the Midcourse Space Experiment (MSX). The number of MSX point sources lying within each clump's 50% peak contour is given in Tables 1 and 2. The density of MSX point sources within the $> 3\sigma$ 850 μm emission region of our map is 50% greater than that in the local field, so we estimate that approximately one third of the 37 sources within the $> 3\sigma$ boundary are likely to be physically associated with the M17 dust continuum clumps. In total, we find 18 MSX point sources that are spatially coincident with 16 of our clumps, and we conclude that most of these MSX sources are probably physically associated with the submillimeter-emitting material. Clumps which are coincident with MSX point sources are labeled with star symbols in Figures 1 and 2.

We would expect clumps which have an embedded mid-infrared source to be among the hotter clumps, but this is only true in 2 of the 16 cases (clump SMM 51 in the center-north and SMM 98 in the southeast). Interestingly, 11 of the 16 clumps with coincident MSX point sources have estimated temperatures less than 20 K. One possible interpretation is that these are cold clumps which have recently formed a hot, compact object. Another possibility is that the flux ratio ceases to be a good measure of clump temperature in the presence of an embedded infrared source. In

some cases, the alignment of an MSX source with a clump probably coincidental.

There are very few candidates in the literature for massive pre-stellar cores. Of the 98 objects for which we were able to estimate temperatures, 39 have $T_{\rm dust} \leq 20$ K and are not coincident with an MSX point source. The masses of these clumps range from 1.13 to 100 $M_\odot$, indicating that they may become low, intermediate, or high-mass stars. While it is certainly possible that deeper infrared observations may reveal the presence of embedded sources within any of these clumps (see, for example, Young et al. 2004), these cold, apparently starless clumps represent the best candidates for massive pre-stellar cores in M17.

4.   THE MASS-RADIUS RELATIONSHIP OF THE M17 CLUMPS

By examining the relationship between the masses and radii of the M17 clumps, we may estimate the degree to which the sample is incomplete and determine something about the clumps' sources of support against collapse. Because the majority of the clumps in our map are at least minimally resolved, the detection threshold must be expressed as a limiting surface brightness, not as a limiting integrated flux or an equivalent clump mass. When the detection threshold is a limiting surface brightness, the clump sample may be incomplete to varying degrees at all masses: even a very massive clump may escape detection if its flux is spread sufficiently thinly. The complex interaction between the limiting surface brightness and the actual, but unknown, distribution of clump masses makes it difficult to constrain the effects of incompleteness in submillimeter continuum clump studies. The mass-radius plot helps to visualize the problem. In Figure 3, we plot the mass of each clump versus its deconvolved effective radius. For both the 850 μm (upper panel) and 450 μm (lower panel) clumps, we use the masses calculated assuming a uniform clump temperature of 30 K and plot only the clumps with no coincident infrared source.

We used these mass-radius plots to test whether the clump sample is essentially 100% complete above the plotted detection threshold or whether the degree of completeness decreases as we approach the threshold from above. The test consists of comparing the number of clumps extracted from a less sensitive version of our map to the number we would expect to extract based on the corresponding detection threshold drawn on Figure 3. We made an 850 μm map using one fifth of the total integration time. Drawing a corresponding detection threshold on the top panel of Figure 3 (not shown), we find that we expect to lose 13 clumps in the less sensitive map. After processing the less sensitive map in the same way as the original map, we find that we lose 16 clumps. Thus, we conclude that the clump sample is close to complete above the detection threshold. This suggests that, apart from potential sources of incompleteness such as chopping, the data are probably close to complete above the detection threshold.

How should we interpret the distribution of clumps in the mass-radius plot? If the clumps were an ensemble of critical Bonnor-Ebert spheres (i.e. thermally supported, pressure-bounded, self-gravitating, and on the verge of collapse), we would expect their mass-radius relationship to be

well-fit by a power law of the form $M \propto R$ (Ebert 1955; Bonnor 1956). Studies of the mass-radius relationship of submillimeter clumps in low-mass star-forming regions such as ρ Oph and Orion B have found good agreement with the $M \propto R$ power law (Motte et al. 2001). Similarly, if the clumps were an ensemble of critical, non-thermally supported spheres, such the logatropic spheres of McLaughlin & Pudritz (1996), then they ought to obey a relationship more like $M \propto R^2$. In Paper I, we found that the 850 μm clumps in NGC 7538 were best fit by a power law, $M \propto R^x$, with exponent $x = 2.1 \pm 0.1$, suggesting that they are primarily turbulently supported. Both of these results are somewhat surprising because, taken at face value, they imply an implausible scenario in which most of the clumps hover somewhere near criticality.

In the present work, refinements to our fitting technique require a more complex interpretation of the M17 clump mass-radius relationship. If we fit the mass-radius relationship of all of the clumps, taking no account of their radius uncertainties and making no distinction between resolved and unresolved clumps, we find results similar to those found in NGC 7538 (Paper I): the 850 μm and 450 μm mass-radius relationships have exponents of $x = 1.5 \pm 0.1$ and $x = 1.9 \pm 0.1$, respectively. However, if we exclude all those clumps with deconvolved radii smaller than the beam radius (those to the left of the vertical dashed line in Fig. 3) and use both the mass and radius uncertainties in computing the fit, we find $x = 4.4 \pm 0.2$ for the 850 μm clumps and $x = 2.6 \pm 0.1$ for the 450 μm clumps. The steepness of the 850 μm mass-radius relationship in M17 is surprising, though it depends sensitively on the precision with which we can measure the radii of the smallest clumps. In principle, the 450 μm data, with twice the linear resolution of the 850 μm data, should produce a more reliable value of the exponent, x. The x value of 2.6 ± 0.1 is much closer to those obtained in similar studies of low-mass star-forming regions. It is unclear, however, whether those studies also accounted for the potentially significant radius uncertainties and therefore whether their results are comparable with ours. Further uncertainties may arise due to incompleteness and unresolved substructure in some clumps. Neither effect can be reliably accounted for at present. Assuming that the value $x = 2.6 \pm 0.1$ from the 450 μm mass-radius relationship is correct, it indicates that the clumps are intermediate between constant surface density ($x = 2$) and constant volume density ($x = 3$), and that they are non-thermally supported.

5. THE M17 CLUMP MASS FUNCTION

5.1. Fitting the M17 Clump Mass Function

Astrophysical mass functions are commonly constructed in two ways: differential ($\Delta N/\Delta M$), in which the data are binned by mass, and cumulative ($N(> M)$), in which the data are not binned. We consider both forms, as each has unique merits. The binning process inherent in the differential mass function (DMF) naturally averages out errors and enables straightforward accounting of uncertainties, but the relatively arbitrary assignment of bin widths and centers introduces bias and can obscure physically significant features of the mass function. The cumulative mass function

(CMF) does not average out errors, but it also does not lose information to binning, an effect which has been found problematic in studies of the stellar mass function (Scalo 1998; Maíz Apellániz & Úbeda 2005). Lack of binning makes the treatment of uncertainties somewhat more complicated in the case of the CMF. In the limit of very many objects ($N \rightarrow \infty$), the differential mass function might be preferable. However, studies of the clump mass function are typically in the relatively small N regime, where neither form of the mass function should be considered definitive and careful consideration of both forms is warranted.

We have constructed both forms of the mass function for the M17 clumps detected in each waveband. Figure 4 shows the differential mass function of the M17 clumps at 850 and 450 μm. To minimize uncertainties caused by the choice of bin width, we have followed the prescription of Maíz Apellániz & Úbeda (2005) and used a variable bin width with a constant number of clumps per bin. Figure 5 shows the cumulative mass function of the M17 clumps in both wavebands. Because we are primarily interested in the mass function of pre-stellar clumps, we exclude from the analysis clumps which are spatially coincident with MSX point sources (as per the discussion of §3.4). In the literature on low-mass pre-stellar cores, the differential version of the core mass function is typically fit using a double power law of the form:

$$\frac{\Delta N}{\Delta M} \propto \left\{ \begin{array}{ll} M^{\alpha_{\mathrm{low}}} & , \ M < M_{\mathrm{break}} \\ M^{\alpha_{\mathrm{high}}} & , \ M \geq M_{\mathrm{break}} \end{array} \right. \tag{4}$$

where α_{low}, α_{high}, M_{break}, and a normalization factor may all be fitted parameters. For the cumulative form of the mass function, the double power law fit takes the form:

$$N(> M) \propto \left\{ \begin{array}{ll} M^{\alpha_{\mathrm{low}}+1} & , \ M < M_{\mathrm{break}} \\ M^{\alpha_{\mathrm{high}}+1} & , \ M \geq M_{\mathrm{break}} \end{array} \right. \tag{5}$$

where the symbols have the same meanings as in Equation 4. In both forms, the exponent of the Salpeter mass function would be $\alpha_{\mathrm{high}} = -2.35$ (Salpeter 1955). In the top rows of Figures 4 and 5, we show fits to double power laws of the forms given in Eqs. 4 and 5. In each fit, α_{low}, α_{high}, M_{break}, and the normalization factor are unconstrained parameters, fitted simultaneously.

To fit the DMF, we used a standard nonlinear Levenberg-Marquardt least squares algorithm (Press et al. 1992), with Poisson error bars, as shown, used for the weights. Poisson error bars are not suitable for fitting the CMF, however, because it is not binned. Instead, we used a Monte Carlo technique to compute the best fit parameters, their uncertainties, and a measure of the goodness-of-fit. For each data set, we generate 10^5 synthetic data sets by randomly varying the mass of each clump within a Gaussian probability envelope whose mean and standard deviation are equal to the observed clump mass and its random uncertainty, respectively. Each of the 10^5 synthetic data sets is then fit using the Levenberg-Marquardt nonlinear least-squares algorithm. To compute approximate weights used in the calculation and minimization of χ^2, we begin by noting that, to

a good approximation, the observed random mass errors scale as $\sigma_M \propto M$. If we approximate the CMF by a power law $N(> M) \simeq AM^{-x}$, then we find the following by partial differentiation:

$$\sigma_N \simeq A(-x)M^{-x-1}\sigma_M \propto N \quad . \tag{6}$$

Thus, we take the statistical weight of each point in the mass function to be $1/\sigma_N^2 \simeq 1/N^2$, which accords with our intuition that clumps of higher masses (lower N in the CMF) should be more heavily weighted. Using this technique, we fit each of the 10^5 synthetic data sets, plot histograms of the best fit parameters, and report the peak of each parameter distribution as the best fit to the observed mass function. The uncertainties on the CMF fits are taken to be the 95% (2 σ) confidence intervals on either side of the best fit parameters. Histograms of the fitted parameters from the Monte Carlo distributions are shown in Figure 6; where the distribution of parameters is nearly symmetric, we quote equal upper and lower uncertainties. The best fit parameters calculated according to this Monte Carlo technique are summarized in Table 3.

Both forms of the 450 μm mass function are well fit over most of their mass range by two power laws with a break at $\sim 19 M_\odot$. The 850 μm DMF is also well fit by two power laws with a slightly lower break mass ($9 \pm 3 \ M_\odot$). The 850 μm CMF, however, is not very well fit by a double power law, as evidenced by the bimodal parameter distribution which results when we attempt a double power law fit (see Fig. 6). The higher of the two peaks in each parameter distribution represent the best fit to a double power law with a break mass at roughly the same position as the break found in the 450 μm mass function ($\sim 19 M_\odot$). The lower peak demonstrates that a third power law with a steeper slope at masses above $\sim 40 M_\odot$ is required to produce a good fit. A mass function might be well fit by two power laws because it is incomplete at low masses or because there is a real physical break in the distribution of clump masses. However, that a a power law fit in three segments is required to produce a good fit suggests that the power laws are merely approximating an unknown continuous distribution. We consider this possibility next.

As will be discussed more extensively in Paper III, the lognormal distribution is a likely candidate for a continuous clump mass distribution. The Galactic field star IMF can be fit by a lognormal mass distribution (Miller & Scalo 1979; Chabrier 2003, but see Scalo 1998 for a dissenting view), as can the mass function of pre-stellar clumps obtained from hydrodynamic simulations (Klessen 2001). Moreover, several analytic studies of the functional form of the clump mass function have found the lognormal distribution to be a viable candidate (Larson 1973; Zinnecker 1984; Adams & Fatuzzo 1996). In the bottom row of Figure 4, we fit the M17 DMFs with a lognormal mass function of the form:

$$\frac{\Delta N}{\Delta M} = \frac{1}{A_1 \sqrt{2\pi} M} \exp\left[-\frac{(\ln M - A_0)^2}{2A_1^2} \right] \quad . \tag{7}$$

Similarly, in the bottom row of Figure 5, we fit the CMFs with the cumulative form of the above clump mass distribution,

$$N(>M) = \frac{1}{2}\left[1 - \text{erf}\left(\frac{\ln M - A_0}{\sqrt{2}A_1}\right)\right] \quad . \tag{8}$$

The best fit values of A_0 and A_1 accompany each plot.

Interestingly, both the 850 and 450 μm CMFs are well fit by a lognormal clump mass distribution. The cumulative distribution function of χ^2 values from our Monte Carlo simulations of the data allow us to determine the probability, P, of obtaining by chance fits as poor as our best fits. The P value for each fit is shown in Figure 5, where $0 < P < 1$. In all cases, both power law and lognormal mass distributions generate acceptable fits ($P \gtrsim 0.1$; Press et al. 1992). As suggested above, the continuous lognormal distribution provides a better fit to the 850 μm CMF than does the double power law. Conversely, the double power law provides a better fit to the 450 μm CMF than the lognormal distribution, though both fits are good. Based on these results, we suggest that both the lognormal distribution and the double power law are viable functional forms for the mass function of the pre-stellar clumps in M17. It is interesting to note that the lognormal distribution produces a good fit to the CMFs using only 2 parameters (mean mass and width), whereas the double power law requires 4 parameters (two exponents, a break point, and a normalization) to produce fits of comparable quality.

Does the quality of the lognormal fits reflect the true distribution of the clump masses, or is it merely coincidence that an intrinsically power-law mass function is reasonably well fit by a lognormal distribution? Experimentation with synthetic data sets quickly reveals that, given sufficient freedom in selecting values of α_{low}, α_{high}, and M_{break}, it is possible to generate an intrinsically double power law mass distribution whose CMF is significantly better fit by a lognormal distribution than by a double power law. However, the range of parameters for which this is the case are not necessarily reflective of those which characterize real star-forming regions. We would like to determine, in the specific case of M17, the probability that a double power law mass distribution with plausible parameters might appear better fit by a lognormal distribution. To assess this probability, we generated 10^5 synthetic 850 and 450 μm clump mass functions with exactly the mass distributions of our best fit double power laws. The CMF of each synthetic data set was fit with both a double power law and a lognormal distribution. We find that the residuals for the lognormal fit exceed those of the double power law fit in 90% of the trials with the synthetic 850 μm CMFs and 82% of the trials with the 450 μm CMFs. Thus, it appears unlikely that the good quality of our lognormal fits reflects a misrepresentation of an intrinsically double power law mass function in M17. Paper III will include a more comprehensive discussion of the uncertainties inherent in determining the functional form of the clump mass function.

Another interpretation of the lognormal fits to the M17 clump mass function is that severe incompleteness at their low-mass ends distorts what would otherwise be a single power law distribution. Incompleteness would produce a mass function with a shallow low-mass end, potentially causing the lognormal distribution to produce the best fit. However, given that the instruments, data reduction techniques, and analytical methods are very similar in our studies of high-mass star-

forming regions and previous studies of low-mass regions, we believe that incompleteness should affect all of the measured mass functions similarly. Comparison of the mass-radius plots in our Figure 3 with Figure 4 of Motte et al. (2001) shows that, in both cases, the distribution of clumps adheres closely to the detection threshold, suggesting that both studies should be similarly affected by incompleteness. If the clump mass function in low-mass star-forming regions were severely incomplete at the low-mass end, it would spoil good the agreement between the clump and stellar mass functions (see §5.3). The corrected clump mass function would then show a considerable overabundance of pre-stellar clumps below ~ 1 $M_\odot$ compared to the number of low-mass stars in the IMF. Thus, we have no reason to believe that incompleteness should dramatically alter the shape of the clump mass function in low-mass star-forming regions, nor that incompleteness has widely disparate effects on studies of low- and high-mass star-forming regions. Hence, we cannot conclude that the quality of the lognormal fits is due to incompleteness. The mass function of M17 may indeed have a lognormal shape with a peak above 1 $M_\odot$.

5.2.   Comparison to the CO Clump Mass Function

Studies of CO clumps in star-forming regions have typically found mass functions which obey shallower power laws than those of submillimeter continuum clumps spanning the same mass range (Kramer et al. 1998). In Paper I, we compared the power law exponents of both CO and submillimeter continuum mass functions and found them to be genuinely discrepant. The evidence from M17 further supports this conclusion. Kramer et al. (1998) found that the mean power-law exponent of the differential mass functions of CO clumps in 7 star-forming regions whose clumps span 10^{-4}–$10^4 M_\odot$ is -1.69 ± 0.02. Stutzki & Güsten (1990) found that the DMF of CO clumps in the M17SW region, which adjoins but does not overlap the region we mapped, is well fit over the mass range M $\simeq$ 10–2000 $M_\odot$ by a single power law with exponent -1.72 ± 0.15. In M17, where the mass function of submillimeter continuum clumps spans a compatible range of ~ 10–$120 M_\odot$, we find a mean power law exponent of $\alpha_{\text{high}} = -2.3 \pm 0.4$. Again, the submillimeter continuum and CO mass functions appear to disagree. In Paper III, we will present an analysis of the functional form of the submillimeter continuum mass function which suggests that it is not well fit by a single power law, as the CO mass functions clearly are. The reason for the discrepancy between the CO and submillimeter continuum mass functions is not yet clear. To help resolve this nagging issue, it would be illuminating to compare the mass functions of objects extracted from CO and submillimeter continuum maps of identical regions, at comparable spatial resolutions, using the same clump extraction technique. For the moment, the issue remains unresolved.

5.3.   Comparison to the Stellar IMF and the Mass Function of Low-Mass Clumps

The masses of the M17 clumps span the high-mass end of the stellar mass range. The masses computed assuming a constant dust temperature range from 0.8 to 160 $M_\odot$, although only a

few clumps have masses $> 100\ M_\odot$. Their deconvolved radii span the range ~ 0.02–0.2 pc, or ~ 4000–40000 AU. Although the large distance to M17 makes it difficult to match the linear resolution and mass sensitivity of similar studies of low-mass star-forming regions, there is significant overlap. For example, in their study of the dust continuum clumps in the Orion B complex, Johnstone et al. (2001) found clumps with masses and radii in the ranges 0.06–30 $M_\odot$ and 3100–20000 AU, respectively. The properties of our clumps also overlap, to differing extents, with those found in the submillimeter continuum studies of ρ Oph (Motte et al. 1998; Johnstone et al. 2000), the Lagoon Nebula (Tothill et al. 2002), and NGC 7538 (Paper I), among others. Based on their masses, sizes, and estimated temperatures, it is reasonable to suggest that some fraction of the "clumps" in M17 are in fact star-forming "cores" which may be the direct precursors of individual stars or small multiple systems. Thus, as has been done in studies of the clump mass function in low-mass star-forming regions, it is reasonable to compare the M17 clump mass function to the mass function of stars in young clusters. Ideally, because we do not know how many stars may form in any given clump, we would compare our clump mass function to the IMF of stellar *systems* in young clusters. The IMF of stellar systems differs from the IMF of individual stars by corrections for unresolved binaries and higher order multiples. In practice, because these corrections are difficult to determine accurately, many published "stellar" IMFs include unresolved systems (Kroupa 2002).

The exact form of the stellar mass function in young clusters is not yet well established, particularly for cluster ages $\lesssim 10^6$ yr (Chabrier 2003). The present-day mass function of young cluster stars can be represented by a lognormal distribution below $\sim 1\ M_\odot$ and a power law above, though whether there may be multiple power law segments at higher masses is not clear. (The IMF of Galactic field stars, for example, is well fit by three power law segments above 1 $M_\odot$; Chabrier 2003.) Where a single high-mass power law is assumed, its exponent is found to be roughly equal to the Salpeter value, i.e. $\Delta N/\Delta M \propto M^{-2.3}$ (Salpeter 1955; Kroupa 2002; Chabrier 2003). Measurements of $\alpha_{\rm high}$ for the stellar mass function of young clusters exhibit substantial variation, ranging at least between -1.5 and -3. (Kroupa 2002) have suggested that, because most measured $\alpha_{\rm high}$ values are approximately normally distributed around -2.3, the spread may be due to ordinary measurement variation. However, other authors favor a steeper value for $\alpha_{\rm high}$, perhaps closer to -3, for massive stars (Sagar & Richtler 1991; Casassus et al. 2000). Studies of the pre-stellar core mass function in low-mass star-forming regions have shown peak masses ($\lesssim 0.5\ M_\odot$) and power law exponents for $M_{\rm clump} \gtrsim 1\ M_\odot$ which agree well with those found in the young cluster stellar IMF (Testi & Sargent 1998; Motte et al. 1998; Johnstone et al. 2000, 2001; Motte et al. 2001). This agreement between the core mass function and the stellar IMF has been widely interpreted as suggesting that the cores are the immediate precursors of stars, and that the core mass function will translate smoothly into a similarly-shaped stellar IMF.

Our four measures of $\alpha_{\rm high}$ for the M17 clumps have much the same characteristics as measures of $\alpha_{\rm high}$ for the stellar IMF. As shown in Table 3, the $\alpha_{\rm high}$ values range between -1.5 and -3.0, with a mean of -2.3±0.4, consistent with the Salpeter value. As with measures of $\alpha_{\rm high}$ for the stellar IMF, variations among the measures of $\alpha_{\rm high}$ for the M17 clump mass function are likely

attributable to ordinary measurement variation. In particular, the uncertain placement of the break between the two power laws can strongly influence the derived power law exponents. Even though we find a mean power-law exponent which agrees with the Salpeter value, this does not necessarily mean that the M17 clump mass function is well-represented by a single power law at high masses. Indeed, as discussed in §5.1, the high-mass end of the 850 μm CMF is best fit by 2 separate power law segments. Thus, the apparent agreement with the Salpeter power law may be misleading: in particular, our good lognormal fits suggest that the structure of the clump mass function is probably somewhat more complicated than this agreement would suggest.

The mass function of high-mass stars in young clusters is typically assumed to have a power law form, so lognormal fits to it are scarce. The IMF of Galactic field stars is presumed lognormal below ~ 1 $M_{\odot}$, with a peak near 0.1 $M_{\odot}$, but it may also be well fit by a lognormal distribution at masses above 1 $M_{\odot}$ (Miller & Scalo 1979; Chabrier 2003, although see Scalo 1998). As mentioned above, studies of the clump mass function in low-mass star-forming regions have typically found that it peaks well below 1 $M_{\odot}$, at several 0.1 $M_{\odot}$ (Testi & Sargent 1998; Motte et al. 1998; Johnstone et al. 2000, 2001; Motte et al. 2001). The range of clump masses probed by these studies typically ranges from a few 0.01 $M_{\odot}$ to as much as 30 $M_{\odot}$. All of our lognormal fits to the M17 clump mass function (both wavelengths, both forms of the mass function) indicate that it peaks above 1 $M_{\odot}$. The fitted peak masses, shown in Table 3, range from 2 to 5.7 $M_{\odot}$ with a mean of 4.2 ± 0.7 $M_{\odot}$, while the clump masses themselves span the range $\sim$1–150 $M_{\odot}$. This suggests that the M17 mass function is not simply the extension to higher masses of the clump mass function seen in low-mass star-forming regions. This hypothesis is supported by our finding that the clump mass functions in both M17 and NGC 7538 (Paper I) are clearly best fit by more than one power law above 1 $M_{\odot}$. The position of the peak mass in each clump mass function is affected by incompleteness, though the extent of this effect is difficult to assess. Furthermore, the differing assumptions made in each study about the clump temperatures and dust emissivities affect the derived value of the peak clump mass. Subject to these caveats, we suggest that the clump mass function in high-mass star-forming regions may be a *scaled-up* version of the low-mass clump mass function. The two may have a common form (perhaps lognormal) but different intrinsic scales, as characterized by their differing peak masses.

6. SUMMARY

We have produced 850 μm and 450 μm SCUBA continuum maps of an approximately $12' \times 12'$ region of the M17 star-forming region, including the source M17N. We used *clfind2d* to extract the clumps from each map, making appropriate corrections for radio continuum contamination and the JCMT error beam. We computed the mean spectral index, α, for each clump and thereby estimated their mean dust temperatures. We computed the mass of each clump using both the calculated temperatures and a universal mean temperature of 30 K. We used MSX data to make a preliminary determination as to which clumps have embedded sources and which are starless. Our

main findings can be summarized as follows:

1. We identify 121 clumps at 850 μm and 101 at 450 μm. Of the 850 μm clumps, 105 are found not to be associated with an MSX point source within their half-peak flux contours. Of the 450 μm clumps, 96 are not coincident with an MSX point source. Assuming a constant dust temperature of 30 K, the 850 μm clump masses span the range 0.8–120 $M_\odot$ and the 450 μmclump masses span the range 1.8–160 $M_\odot$.

2. By combining the 450 μm and 850 μm data for each clump with the assumption of a constant dust emissivity index, β, we derive a mean spectral index, α, and dust temperature, $T_{\rm dust}$ for each clump detected at 850 μm. The spectral indices range from 0.45 to 3.45, with a mean of 2.74. The estimated dust temperatures range from 6 to 235 K, with a mean of 33 K and a median of 20 K. As in Paper I, we find a correlation between high spectral index and high submillimeter continuum flux.

3. Fitting the mass-radius relationship of the clumps to a power law, $M \propto R^x$, we find $x = 4.4 \pm 0.2$ for the 850 μm clumps and $x = 2.6 \pm 0.1$ for the 450 μm clumps. In both wavebands, the distribution of clumps in mass-radius space adheres fairly close to the detection threshold, which is of the form $M \propto R^2$, making it difficult to assess the effects of incompleteness. If the observed mass-radius relationship accurately reflects the characteristics of the M17 clumps, we suggest that it implies that they derive significant support from nonthermal motions.

4. We have identified 39 "cold" clumps ($T_{\rm dust} \lesssim 20$ K) which are not spatially coincident with an MSX point source. We suggest that these are the best candidates for very young massive pre-protostellar cores in the mapped portion of M17.

5. We have produced both differential ($\Delta N/\Delta M$) and cumulative ($N(> M)$) mass functions for the "starless" clumps detected in each waveband. We fit each mass function with both a segmented power law and a lognormal distribution. All forms of the mass function are well fit by a double power law except the 850 μm CMF, which would require three power law segments for a good fit. The mean power-law exponent of the high-mass end of the clump mass function is $\alpha_{\rm high} = -2.4 \pm 0.3$. On the same scale, the Salpeter value would be $\alpha_{\rm high} = -2.35$.

6. We suggest the lognormal distribution as a candidate continuous form for the clump mass function in M17. The lognormal distribution fits the M17 mass function as well as or better than the commonly-used double power law, and with fewer fitted parameters (2 instead of 4). The lognormal distribution also eliminates the need to invoke a physically unmotivated third power law segment to obtain a good fit to the 850 μm CMF. A lognormal mass function would be consistent with the view of high-mass star formation as an inherently clustered, and therefore highly stochastic phenomenon (e.g. Adams & Fatuzzo 1996). The mean peak mass of the fitted lognormal distributions is 3.8 ± 0.7 $M_\odot$, which assumes a dust emissivity of β

$= 1.5$ and a mean dust temperature of $T = 30$ K. This mass is substantially higher than the peak mass obtained from fits to the stellar IMF and low-mass clump mass function, which is typically a few tenths of a solar mass.

7. We suggest that the clump mass function in massive star-forming regions may be a scaled-up version of the mass function seen in low-mass star-forming regions, such as ρ Oph and Orion B. The general shape of the mass functions appears to be similar, but their intrinsic scales, represented by their peak masses (for example), differ significantly. The issue of the similarity in the shape of the mass function among star-forming regions will be discussed at length in Paper III.

REFERENCES

Adams, F. C., & Fatuzzo, M. 1996, ApJ, 464, 256

Bonnell, I. A., Bate, M. R., Clarke, C. J., & Pringle, J. E. 1997, MNRAS, 285, 201

Bonnell, I. A., Bate., M. R., Clarke, C. J., & Pringle, J. E. 2001a, MNRAS, 323, 785

Bonnell, I. A., Clarke, C. J., Bate, M. R., Pringle, J. E. 2001b, MNRAS, 324, 573

Bonnell, I. .A., & Bate, M. .R. 2002, MNRAS, 336, 659

Bonnor, W. G. 1956, MNRAS, 116, 351

Brogan, C. L., & Troland, T. H. 2001, ApJ, 560, 821

Casassus, S., Bronfman, L., May, J., & Nyman, L.-Å 2000, A&A, 358, 514

Chabrier, G. 2003, PASP, 115, 763

Chini, R., & Wargau, W. F. 1998, A&A, 329, 161

Chini, R., Nielbock, M., & Beck, R. 2000, A&A, 357, L33

Dupac, X., et al. 2002, A&A, 392, 691

Ebert, R. 1955, Z. Astrophys., 37, 217

Emerson, D. T. 1995, in ASP Conf. Ser. 75, Multi-Feed Systems for Radio Telescopes, ed. D. T. Emerson & J. M. Payne (San Francisco: ASP), 309

Felli, M., Massi, M., & Churchwell, E. 1984, A&A, 136, 53

Hanson, M. M., Howarth, I. D., Conti, P. S. 1997, ApJ, 489, 698

Henning, Th., Klein, R., Launhardt, R., Lemke, D., & Pfau, W. 1998, A&A, 332, 1035

Hildebrand, R. H. 1983, QJRAS, 24, 267

Jaffe, D. T., Güsten, & Downes, D. 1981, ApJ, 250, 621

Johnstone, D. J., Wilson, C. D., Moriarty-Schieven, G., Joncas, G., Smith, G., Gregersen, E., & Fich, M. 2000, ApJ, 545, 327

Johnstone, D. J., Fich, M., Mitchell, G. F., Moriarty-Schieven, G. 2001, ApJ, 559, 307

Kerton, C. R., Martin, P. G., Johnstone, D., & Ballantyne, D. R. 2001, ApJ, 552, 601

Klessen, R. S. 2001, ApJ, 556, 837

Klessen, R., & Burkert, A. 2000, ApJS, 128, 287

Klein, R., Henning, Th., & Cesarsky, D. 1999, A&A, 343, L53

Kramer, C., Stutzki, J., Röhrig, R., & Corneliussen, U. 1998, A&A, 329, 249

Kroupa, P. 2002, Science, 295, 82

Krumholz, M. R., McKee, C. F., & Klein, R. I. 2005, ApJ, 618, 33

Lada, C. J. 1976, ApJS, 32, 603

Lada, C. J., Dickinson, D. F., Gottlieb, C. A., & Wright, E. L. 1976, ApJ, 207, 113

Larson, R .B. 1973, MNRAS, 161, 133

Maíz Apellániz, J. & Úbeda L. 2005, ApJ, 629, 873

McKee, C. F., & Tan, J. C. 2002, Nature, 416, 59

McKee, C. F., & Tan, J. C. 2003, ApJ, 585, 850

McLaughlin, D. E. & Pudritz, R. E. 1996, ApJ, 469, 194

Miller, G .E., & Scalo, J. M. 1979, ApJS, 41, 513

Mookerjea, B., Kramer, C., Nielbock, M., & Nyman, L.-Å. 2004, A&A, 426, 119

Motte, F., André, P., Ward-Thompson, D., Bontemps, S. 2001, A&A, 372, L41

Motte, F., André, P., & Neri, R. 1998, A&A, 336, 150

Motte, F., Schilke, P., & Lis, D.C. 2003, ApJ, 582, 277

Nielbock, M., Chini, R., Jütte, M., & Manthey, E. 2001, A&A, 377, 273

Press, W. H., Teukolsky, S. A., Vetterling, W. T., & Flannery, B. P. 1992, Numerical Recipes in FORTRAN, (2nd ed.; Cambridge: University Press)

Reid, M. A., & Wilson, C. D. 2005, ApJ, 625, 891

Sagar, R. & Richtler, T. 1991, A&A, 250, 324

Salpeter, E. E. 1955, ApJ, 121, 161

Sandell, G., & Sievers, A. 2004, ApJ, 600, 269

Scalo, J. 1998, in ASP Conf. Ser. 142, The Stellar Initial Mass Function Proceedings, ed. G. Gilmore & D. Howell (San Francisco: ASP), 201

Stutzki, J. & Güsten, R. 1990, ApJ, 356, 513

Testi, L. & Sargent, A. I. 1998, ApJ, 508, L91

Tothill, N. F. H., White, G. J., Matthews, H. E., McCutcheon, W. H., McCaughrean, M. J., Kenworthy, M. A. 2002, ApJ, 580, 285

Williams, J. P., de Geus, E. J., & Blitz, L. 1994, ApJ, 428, 693

Wilson, C. D., Howe, J. E., & Balogh, M. L. 1999, ApJ, 517, 174

Wilson, T. L., Fazio, G. G., Jaffe, D., Kleinmann, D., Wright, E. L., & Low, F. J. 1979, A&A, 76, 86

Young, C. H., et al. 2004, ApJS, 154, 396

Zinnecker, H. 1984, MNRAS, 210, 43
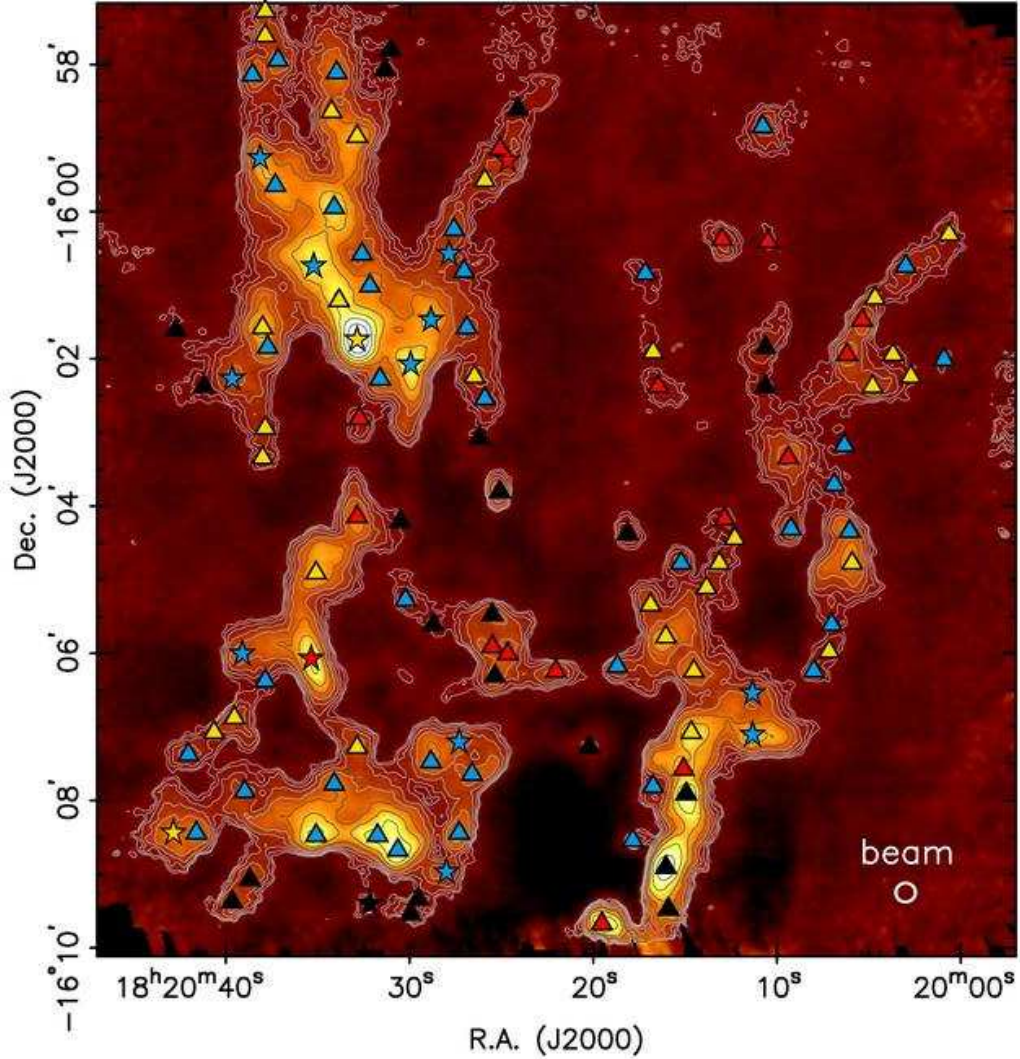
Fig. 1.— Submillimeter continuum image of M17 at 850 μm, in halftone color with logarithmically spaced contours. The contours begin at 3 σ (0.082 Jy beam^{-1}) and increase by factors of 1.5. Triangle and star symbols mark the clump peaks: stars indicate clumps which are spatially coincident with an MSX point source within their half-peak contour; triangles indicate clumps with no coincident MSX point source. Symbol colors reflect a clump's estimated dust temperature: blue for $T_{dust} \leq 20$ K, yellow for 20 K$< T_{dust} \leq 40$ K, red for $T_{dust} > 40$ K, and black for those which lack a reliable temperature estimate. The cross near M17N represents the position and positional uncertainty of the water maser detected by Jaffe et al. (1981).
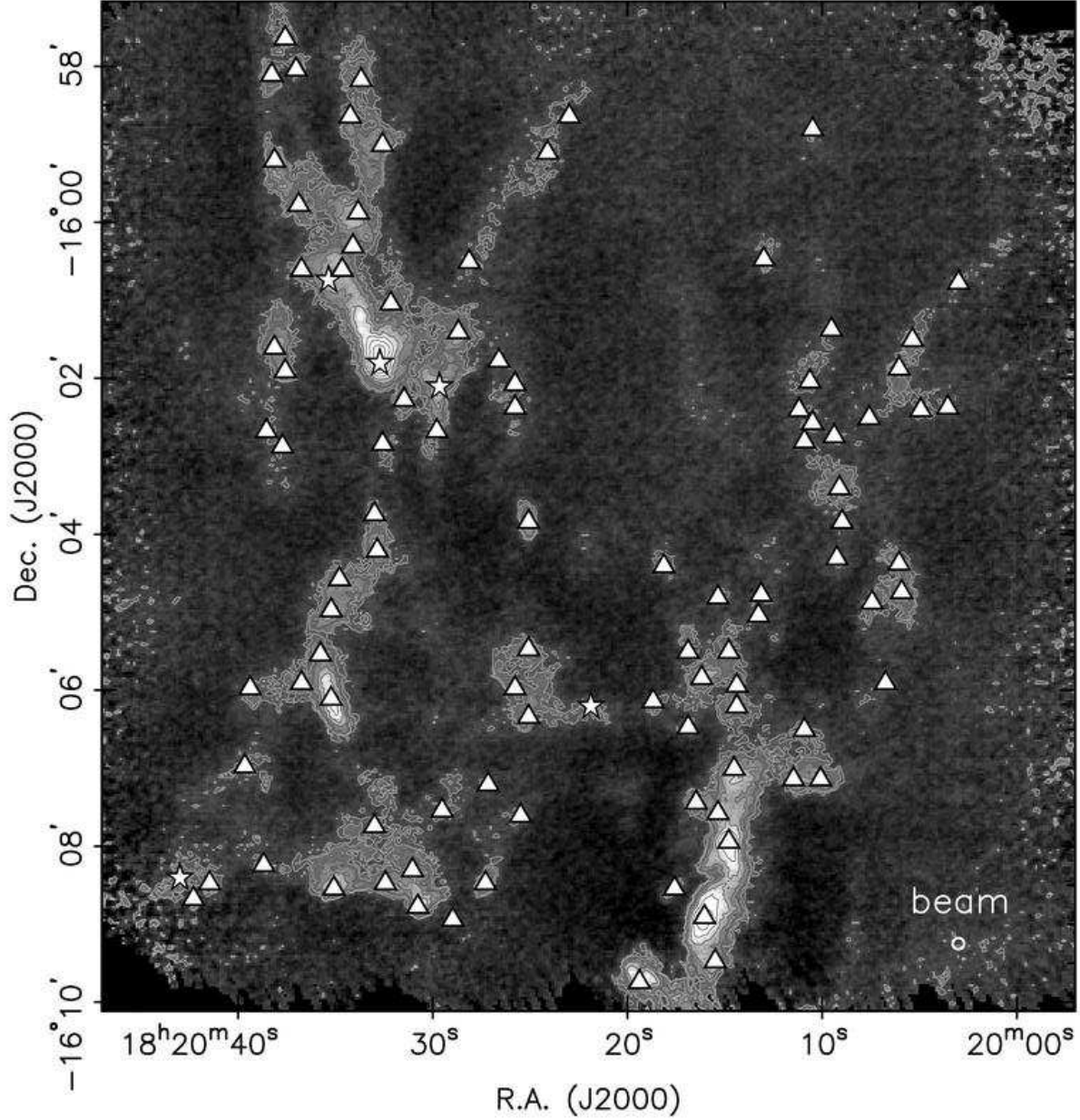
Fig. 2.— Submillimeter continuum image of M17 at 450 μm, in gray scale with logarithmically spaced contours. The contours begin at 3 σ (0.96 Jy beam^{-1}) and increase by factors of 1.5. Triangle and star symbols mark the clump peaks: stars indicate clumps which are spatially coincident with an MSX point source within their half-peak contour; triangles indicate clumps with no coincident MSX point source.
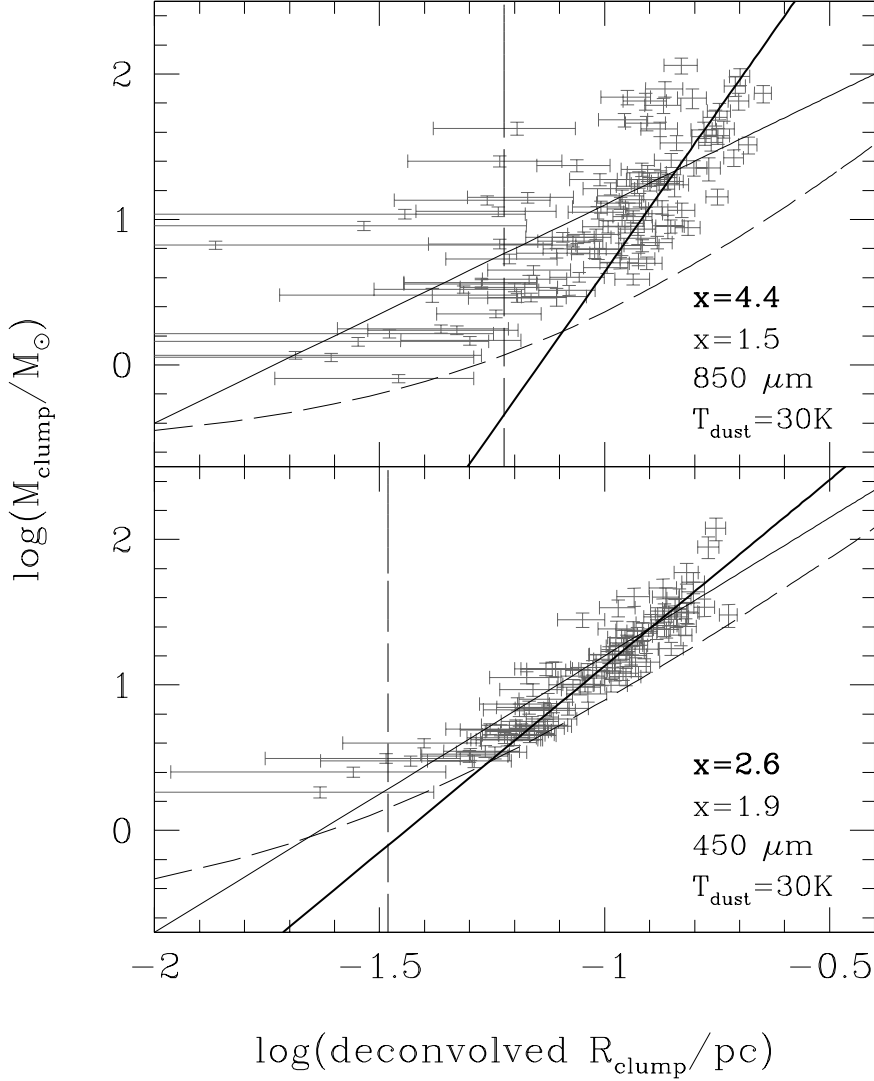
Fig. 3.— The mass-radius relationship for three ensembles of M17 clumps, with masses calculated assuming a uniform clump dust temperature of 30 K. The curving dashed lines represent the detection threshold. The vertical dashed lines represent the beam radius; clumps to the left of this line are unresolved. The plotted error bars represent the random mass uncertainty and the uncertainty on the deconvolved radius assuming a $0.5''$ uncertainty in the beam diameter and a $2''$ (1 pixel) uncertainty in the clump radius before deconvolution. The solid lines represent fits to power laws of the form $M \propto R^x$; the thick line shows a fit only to the resolved clumps and accounting for both their mass and radius uncertainties, while the thin line fits all of the clumps and ignores the uncertainties. The values of the exponent, x, are given for each line in a correspondingly regular/bold typeface.
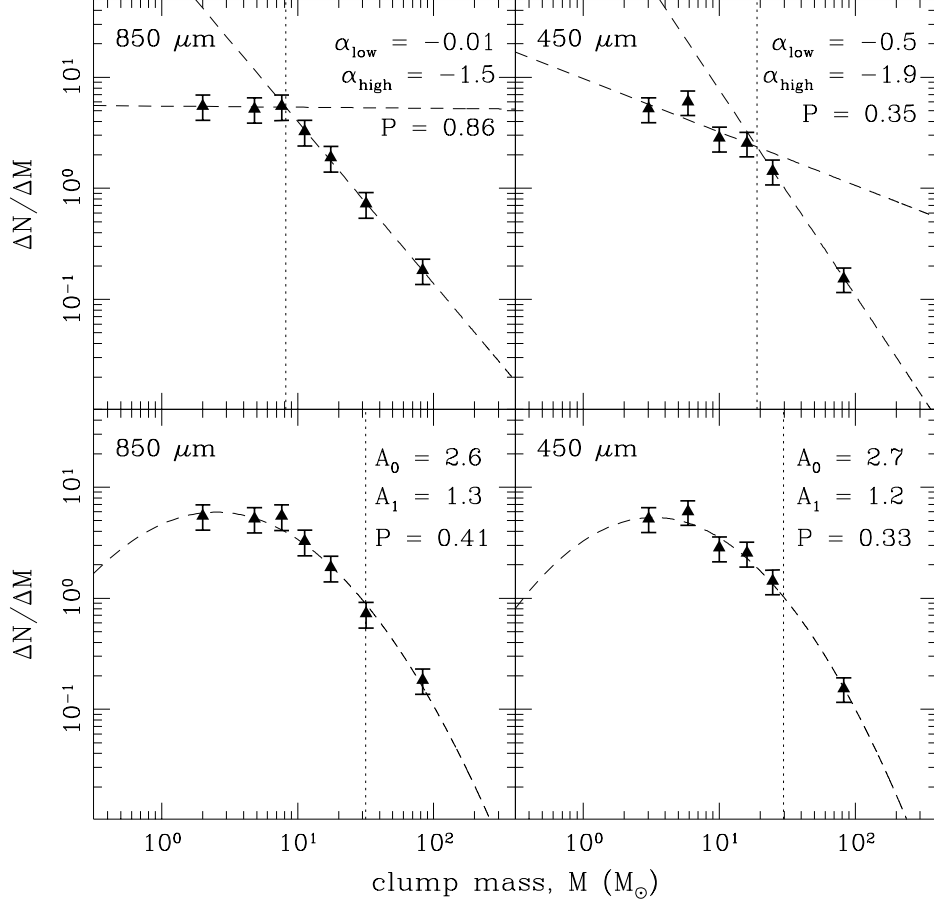
Fig. 4.— Differential mass function for the M17 starless clumps detected at 850 μm (left) and 450 μm (right), with clump masses calculated assuming a constant dust temperature of 30 K. In the top row, the mass functions are fitted with a broken power law (*dashed lines*), whose break (*dotted lines*) is a parameter of the fit. The best fit exponents of the two power laws are shown in the upper right corner of each panel. In the bottom row, the data are fitted with a lognormal shape (*dashed curve*), defined by Eq. 7, with best fit parameters as shown. The vertical dotted line in the lower panels represents the mean mass derived from the lognormal fit. Values for all the fitted parameters, with uncertainties, are given in Table 3.
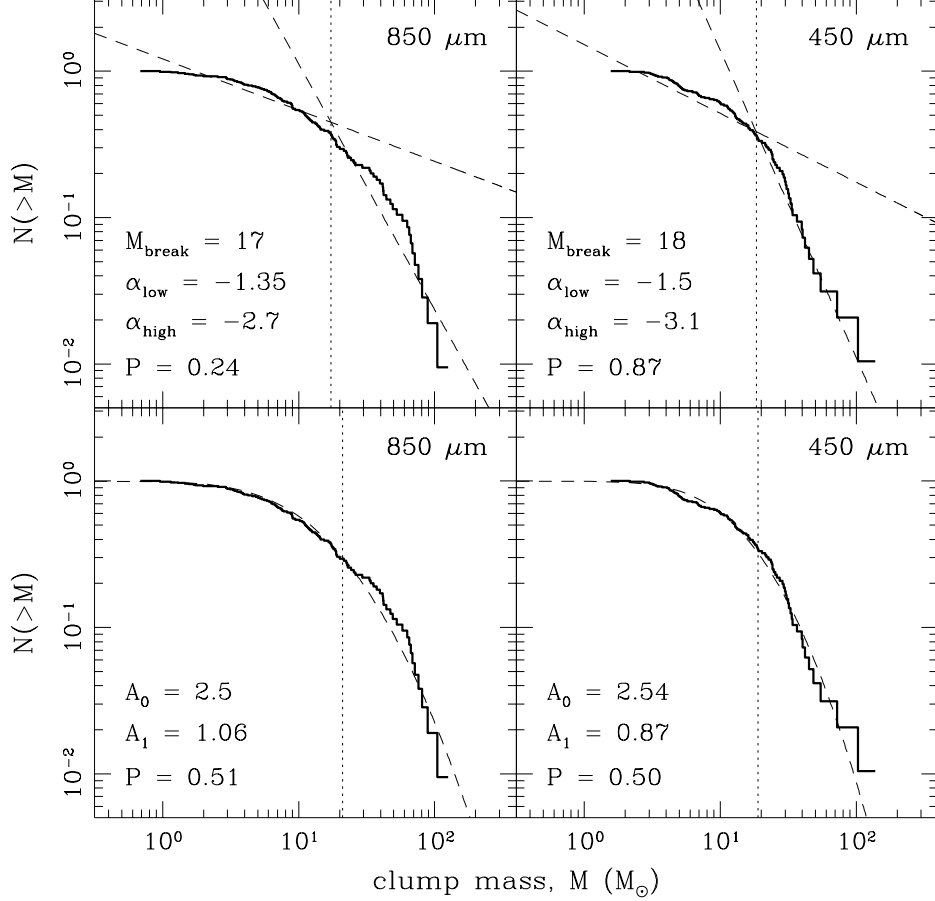
Fig. 5.— Cumulative mass function for the M17 starless clumps detected at 850 (*left*) and 450 μm (*right*), with clump masses calculated assuming a constant dust temperature of 30 K. In the top row, the mass functions are fitted with broken power laws (*dashed lines*), whose break points are also parameters of the fit (*dotted lines*). In the 850 μm CMF, three power laws (not shown) are required to obtain a good fit. For consistency, we show only the fit with two power laws. The exponents of the best fit power laws are shown in the lower left corner of each panel. In the bottom row, the data are fitted to the CMF corresponding to a lognormal DMF (see Eq. 8), with best fit parameters as shown. The vertical dotted line in the lower panels represents the mean mass derived from the lognormal fit. Values for all the fitted parameters, with uncertainties, are given in Table 3. The P values are goodness-of-fit measures, with values $\gtrsim 0.1$ indicating a good fit (see §5.1).
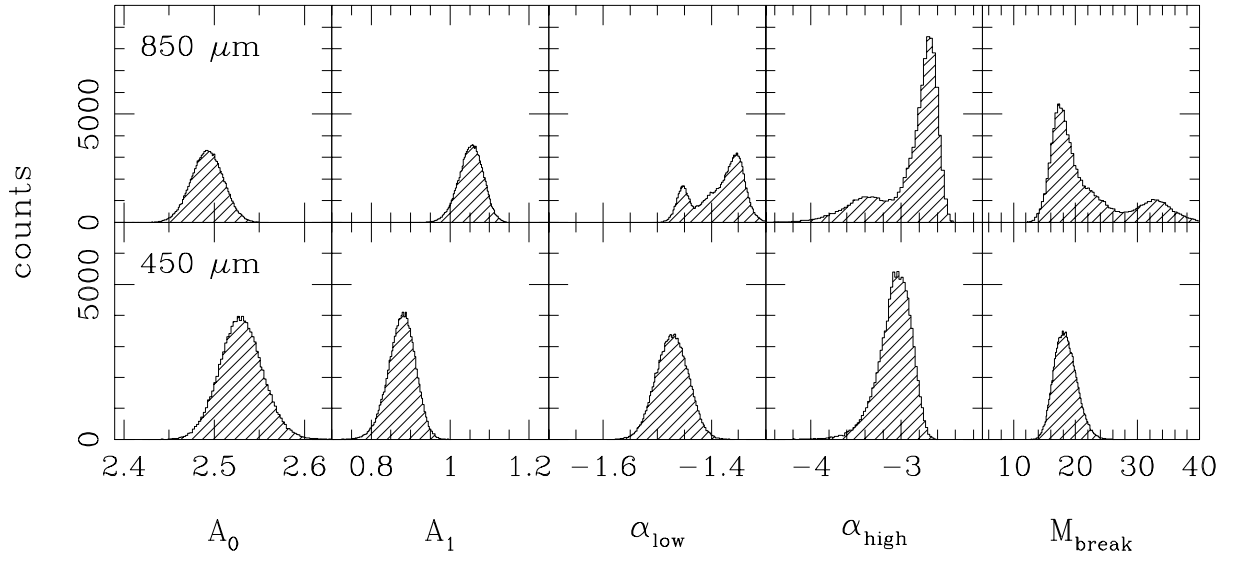
Fig. 6.— Histograms of the best fit parameters derived from lognormal and double power law fits to 10^5 realizations of the M17 cumulative clump mass function within the random uncertainties on each clump mass. Best fit parameter distributions are shown for both the 850 μm CMF (*top row*) and the 450 μm CMF (*bottom row*). In general, the distributions are close to normal, except for the double power law fits to the 850 μm CMF, which are bimodal.

– 27 –

Table 1.   Properties of the 850 μm Clumps

Name (M17-)	R.A. (J2000)	Dec. (J2000)	$R_{\rm eff}$ (pc)	$S_{\rm peak}$[a] (Jy beam^{-1})	$S_{850}^{\rm int}$ [a] (Jy)	$\langle\alpha\rangle$[b]	$\langle T_d\rangle$[c] (K)	$M_{T_d=30K}$[a] ($M_\odot$)	M_{T_d}[a] ($M_\odot$)	$n_{\rm psc}$[d]
SMM1	18 20.0 00.6	-16 00 18	0.12	0.26±0.01	0.45±0.05	2.89	23	7.4±0.8	11±1	0
SMM2	18 20.0 00.9	-16 02 00	0.02	0.12±0.01	0.07±0.01	1.91	10	1.13±0.07	6.4±0.4	0
SMM3	18 20.0 02.7	-16 02 14	0.06	0.15±0.01	0.14±0.01	3.00	27	2.2±0.2	2.6±0.2	0
SMM4	18 20.0 03.0	-16 00 44	0.13	0.32±0.01	0.73±0.08	2.38	14	12±1	40±4	0
SMM5	18 20.0 03.7	-16 01 56	0.06	0.16±0.01	0.17±0.01	3.10	33	2.9±0.2	2.5±0.2	0
SMM6	18 20.0 04.7	-16 01 10	0.06	0.29±0.01	0.32±0.03	2.99	27	5.4±0.5	6.3±0.5	0
SMM7	18 20.0 04.8	-16 02 22	0.14	0.46±0.02	1.1±0.1	3.04	30	18±2	19±2	0
SMM8	18 20.0 05.4	-16 01 28	0.04	0.55±0.02	0.66±0.06	3.35	85	10.9±0.9	3.2±0.2	0
SMM9	18 20.0 05.9	-16 04 46	0.18	0.82±0.03	2.5±0.3	2.85	21	42±6	66±9	0
SMM10	18 20.0 06.1	-16 04 20	0.10	0.64±0.03	1.1±0.1	2.73	19	19±2	37±4	0
SMM11	18 20.0 06.2	-16 01 56	0.13	0.55±0.02	1.2±0.1	3.28	58	19±2	9±1	0
SMM12	18 20.0 06.3	-16 03 10	0.05	0.12±0.01	0.09±0.01	2.75	19	1.5±0.1	2.8±0.2	0
SMM13	18 20.0 06.9	-16 03 42	0.11	0.15±0.01	0.30±0.03	2.67	17	5.0±0.5	10.8±0.9	0
SMM14	18 20.0 07.0	-16 05 36	0.09	0.18±0.01	0.24±0.02	1.54	9	4.0±0.3	33±3	0
SMM15	18 20.0 07.2	-16 05 58	0.05	0.21±0.01	0.22±0.02	3.09	32	3.6±0.3	3.3±0.2	0
SMM16	18 20.0 08.0	-16 06 14	0.06	0.21±0.01	0.21±0.02	2.67	18	3.4±0.3	7.3±0.5	0
SMM17	18 20.0 09.2	-16 04 18	0.10	0.34±0.01	0.54±0.06	2.45	14	8.9±0.9	27±3	0
SMM18	18 20.0 09.4	-16 03 20	0.21	0.55±0.02	2.0±0.3	3.30	63	33±5	13±2	0
SMM19	18 20.0 10.5	-16 00 24	0.05	0.15±0.01	0.10±0.01	3.42	144	1.7±0.1	0.29±0.02	0
SMM20	18 20.0 10.6	-16 01 50	0.15	0.28±0.01	0.70±0.08	3.88	$\cdots$	12±1	$\cdots$	0
SMM21	18 20.0 10.6	-16 02 22	0.15	0.19±0.01	0.53±0.06	3.86	$\cdots$	9±1	$\cdots$	0
SMM22	18 20.0 10.8	-15 58 50	0.18	0.38±0.02	0.9±0.1	2.16	12	14±2	62±8	0
SMM23	18 20.0 11.3	-16 07 06	0.19	1.14±0.05	4.1±0.6	2.79	20	67±9	120±20	1
SMM24	18 20.0 11.3	-16 06 32	0.16	0.51±0.02	1.7±0.2	2.67	18	28±3	60±5	1
SMM25	18 20.0 12.3	-16 04 26	0.04	0.14±0.01	0.11±0.01	3.04	29	1.8±0.1	1.8±0.1	0
SMM26	18 20.0 12.9	-16 04 10	0.07	0.16±0.01	0.18±0.01	3.44	220	2.9±0.2	0.31±0.02	0
SMM27	18 20.0 13.0	-16 00 22	0.10	0.32±0.01	0.48±0.05	3.23	47	7.9±0.7	4.5±0.4	0
SMM28	18 20.0 13.1	-16 04 46	0.07	0.21±0.01	0.27±0.02	2.84	21	4.5±0.4	7.2±0.6	0
SMM29	18 20.0 13.8	-16 05 06	0.11	0.28±0.01	0.54±0.06	2.89	23	9.0±0.9	13±1	0
SMM30	18 20.0 14.5	-16 06 14	0.17	0.66±0.03	2.0±0.3	3.06	30	34±4	34±4	0
SMM31	18 20.0 14.7	-16 07 04	0.14	1.30±0.05	3.7±0.5	3.17	40	61±8	43±5	0
SMM32	18 20.0 14.9	-16 07 54	0.14	2.19±0.09	4.8±0.6	3.58	$\cdots$	80±10	$\cdots$	0
SMM33	18 20.0 15.1	-16 07 34	0.11	1.13±0.05	2.9±0.3	3.31	66	48±5	19±2	0
SMM34	18 20.0 15.2	-16 04 46	0.09	0.33±0.01	0.43±0.04	2.77	20	7.1±0.7	13±1	0
SMM35	18 20.0 15.9	-16 09 28	0.06	0.94±0.04	1.5±0.1	3.65	$\cdots$	25±2	$\cdots$	0
SMM36	18 20.0 16.0	-16 08 54	0.15	3.0±0.1	6.9±0.9	3.59	$\cdots$	110±20	$\cdots$	0
SMM37	18 20.0 16.0	-16 05 46	0.13	1.00±0.04	2.5±0.3	3.18	40	42±5	29±3	0
SMM38	18 20.0 16.5	-16 02 22	0.13	0.20±0.01	0.42±0.04	3.31	67	7.0±0.7	2.7±0.3	0
SMM39	18 20.0 16.7	-16 07 48	0.06	0.31±0.01	0.41±0.03	2.61	16	6.8±0.6	16±1	0
SMM40	18 20.0 16.7	-16 01 54	0.12	0.14±0.01	0.23±0.02	3.10	33	3.9±0.4	3.4±0.3	0
SMM41	18 20.0 16.9	-16 05 20	0.13	0.46±0.02	1.1±0.1	2.87	22	18±2	27±3	0
SMM42	18 20.0 17.2	-16 00 50	0.12	0.17±0.01	0.30±0.03	2.57	16	5.0±0.5	13±1	0
SMM43	18 20.0 17.9	-16 08 32	0.05	0.34±0.01	0.20±0.01	2.16	12	3.3±0.2	14.3±0.8	0
SMM44	18 20.0 18.1	-16 04 22	0.09	0.36±0.01	0.38±0.04	3.62	$\cdots$	6.3±0.6	$\cdots$	0
SMM45	18 20.0 18.7	-16 06 10	0.11	0.40±0.02	0.78±0.08	2.39	14	13±1	42±4	0
SMM46[e]	18 20.0 19.5	-16 09 40	0.06	1.86±0.07	2.5±0.3	3.43	164	42±5	6.1±0.6	0
SMM47	18 20.0 20.2	-16 07 16	0.03	0.14±0.01	0.05±0.01	$\cdots$	$\cdots$	0.81±0.04	$\cdots$	0
SMM48[e]	18 20.0 22.0	-16 06 14	0.10	0.46±0.02	0.67±0.07	3.22	46	11±1	6.6±0.7	0
SMM49	18 20.0 24.1	-15 58 36	0.14	0.20±0.01	0.54±0.06	3.73	$\cdots$	9±1	$\cdots$	0
SMM50	18 20.0 24.7	-16 06 00	0.07	0.53±0.02	0.85±0.08	3.45	235	14±1	1.4±0.1	0
SMM51	18 20.0 24.7	-15 59 18	0.06	0.38±0.02	0.59±0.05	3.31	65	9.8±0.8	3.9±0.3	1
SMM52	18 20.0 25.1	-16 03 48	0.03	0.59±0.02	0.55±0.05	3.58	$\cdots$	9.1±0.8	$\cdots$	0
SMM53	18 20.0 25.1	-15 59 08	0.08	0.29±0.01	0.45±0.04	3.38	105	7.6±0.6	1.8±0.1	0
SMM54	18 20.0 25.4	-16 06 18	0.11	0.55±0.02	0.87±0.09	3.58	$\cdots$	15±2	$\cdots$	0
SMM55[e]	18 20.0 25.5	-16 05 28	0.12	0.49±0.02	1.0±0.1	3.48	$\cdots$	17±2	$\cdots$	0
SMM56	18 20.0 25.5	-16 05 54	0.05	0.50±0.02	0.82±0.07	3.40	126	14±1	2.6±0.2	0
SMM57	18 20.0 25.9	-16 02 32	0.09	0.32±0.01	0.46±0.04	2.71	18	7.6±0.7	15±1	0
SMM58	18 20.0 25.9	-15 59 34	0.12	0.32±0.01	0.66±0.07	3.03	29	11±1	12±1	0
SMM59	18 20.0 26.2	-16 03 04	0.02	0.13±0.01	0.07±0.01	$\cdots$	$\cdots$	1.17±0.07	$\cdots$	0
SMM60	18 20.0 26.5	-16 02 14	0.11	0.33±0.01	0.71±0.07	2.87	22	12±1	18±2	0
SMM61[e]	18 20.0 26.6	-16 07 38	0.14	0.34±0.01	1.0±0.2	2.27	13	17±3	70±10	0
SMM62	18 20.0 26.9	-16 01 34	0.14	0.36±0.01	1.1±0.1	2.18	12	18±2	74±8	0
SMM63	18 20.0 27.0	-16 00 48	0.12	0.25±0.01	0.52±0.05	1.69	9	8.6±0.9	61±6	0
SMM64[e]	18 20.0 27.3	-16 08 26	0.12	0.73±0.03	1.3±0.2	2.72	18	21±3	41±5	0
SMM65[e]	18 20.0 27.3	-16 07 12	0.13	0.58±0.02	1.3±0.2	1.46	8	22±3	200±20	1
SMM66	18 20.0 27.6	-16 00 14	0.12	0.40±0.02	0.82±0.09	2.77	19	14±2	25±3	0

Table 1—Continued

Name (M17-)	R.A. (J2000)	Dec. (J2000)	$R_{\rm eff}$ (pc)	$S_{\rm peak}$[a] (Jy beam^{-1})	$S_{850}^{\rm int}$[a] (Jy)	$\langle\alpha\rangle$[b]	$\langle T_d\rangle$[c] (K)	$M_{T_d=30K}$[a] ($M_\odot$)	M_{T_d}[a] ($M_\odot$)	$n_{\rm psc}$[d]
SMM67	18 20.0 27.9	-16 00 34	0.13	0.42±0.02	1.2±0.1	2.19	12	20±2	83±9	1
SMM68[e]	18 20.0 28.0	-16 08 58	0.12	0.26±0.01	0.5±0.1	0.45	6	9±2	180±30	2
SMM69	18 20.0 28.7	-16 05 36	0.10	0.19±0.01	0.28±0.03	$\cdots$	$\cdots$	4.7±0.4	$\cdots$	0
SMM70	18 20.0 28.8	-16 01 28	0.16	1.07±0.04	4.2±0.6	2.61	16	69±9	170±20	1
SMM71[e]	18 20.0 28.8	-16 07 28	0.17	0.50±0.02	1.4±0.3	2.55	16	23±4	60±10	0
SMM72[e]	18 20.0 29.5	-16 09 20	0.08	0.18±0.01	0.18±0.03	$\cdots$	$\cdots$	2.9±0.5	$\cdots$	0
SMM73	18 20.0 29.9	-16 02 04	0.14	1.49±0.06	4.4±0.6	2.73	19	73±9	140±20	2
SMM74[e]	18 20.0 29.9	-16 09 32	0.04	0.25±0.01	0.18±0.02	$\cdots$	$\cdots$	3.0±0.4	$\cdots$	0
SMM75	18 20.0 30.2	-16 05 16	0.10	0.25±0.01	0.35±0.03	1.66	9	5.8±0.5	43±4	0
SMM76	18 20.0 30.5	-16 04 12	0.08	0.15±0.01	0.20±0.02	$\cdots$	$\cdots$	3.3±0.3	$\cdots$	0
SMM77[e]	18 20.0 30.6	-16 08 40	0.12	1.87±0.07	3.9±0.5	2.44	14	65±9	200±30	0
SMM78	18 20.0 31.0	-15 57 48	0.03	0.16±0.01	0.09±0.01	$\cdots$	$\cdots$	1.4±0.1	$\cdots$	0
SMM79	18 20.0 31.3	-15 58 04	0.12	0.17±0.01	0.32±0.03	$\cdots$	$\cdots$	5.4±0.6	$\cdots$	0
SMM80	18 20.0 31.6	-16 02 16	0.14	0.79±0.03	2.0±0.3	2.69	18	34±4	70±8	0
SMM81[e]	18 20.0 31.7	-16 08 28	0.16	1.29±0.05	4.1±0.7	2.68	18	70±10	140±20	0
SMM82	18 20.0 32.2	-16 01 00	0.12	0.85±0.03	2.8±0.3	2.67	18	46±6	100±10	0
SMM83	18 20.0 32.2	-16 09 24	0.05	0.20±0.01	0.16±0.01	$\cdots$	$\cdots$	2.7±0.2	$\cdots$	1
SMM84	18 20.0 32.6	-16 00 34	0.12	0.53±0.02	1.3±0.1	2.23	12	22±2	87±9	0
SMM85	18 20.0 32.7	-16 02 48	0.11	0.24±0.01	0.38±0.04	3.27	54	6.3±0.7	3.0±0.3	0
SMM86[e]	18 20.0 32.9	-16 01 44	0.14	3.7±0.1	7±1	3.14	37	120±20	90±20	1
SMM87	18 20.0 32.9	-15 58 58	0.18	0.99±0.04	3.3±0.5	2.88	23	55±8	80±10	0
SMM88	18 20.0 32.9	-16 04 08	0.18	0.83±0.03	2.3±0.3	3.19	42	38±5	25±3	0
SMM89	18 20.0 32.9	-16 07 16	0.16	0.52±0.02	1.4±0.2	2.86	22	23±3	35±4	0
SMM90	18 20.0 33.8	-16 01 12	0.11	1.55±0.06	4.2±0.5	2.90	23	69±8	100±10	0
SMM91	18 20.0 34.0	-15 58 06	0.17	0.65±0.03	2.2±0.3	2.76	19	37±5	69±9	0
SMM92	18 20.0 34.1	-15 59 56	0.20	1.20±0.05	5.8±0.8	2.78	20	100±10	170±20	0
SMM93[e]	18 20.0 34.1	-16 07 46	0.17	0.62±0.02	2.5±0.3	2.60	16	41±6	100±10	0
SMM94	18 20.0 34.2	-15 58 38	0.14	0.67±0.03	1.5±0.2	2.82	21	26±3	43±5	0
SMM95[e]	18 20.0 35.1	-16 08 28	0.19	1.41±0.06	5.0±0.8	2.67	17	80±10	180±30	0
SMM96	18 20.0 35.1	-16 04 54	0.23	0.98±0.04	4.4±0.6	3.05	30	70±10	70±10	0
SMM97	18 20.0 35.2	-16 00 44	0.21	1.28±0.05	6.5±0.9	2.79	20	110±20	190±30	1
SMM98	18 20.0 35.4	-16 06 04	0.22	1.55±0.06	5.5±0.8	3.26	53	90±10	45±6	1
SMM99	18 20.0 37.2	-15 57 56	0.10	0.60±0.02	1.0±0.1	2.65	17	16±2	36±3	0
SMM100	18 20.0 37.3	-15 59 38	0.20	0.91±0.04	3.9±0.5	2.49	15	65±9	180±20	0
SMM101	18 20.0 37.7	-16 01 50	0.09	0.93±0.04	1.4±0.1	2.62	17	23±2	55±5	0
SMM102	18 20.0 37.9	-15 57 36	0.06	0.51±0.02	0.68±0.06	2.87	22	11±1	17±1	0
SMM103	18 20.0 37.9	-15 57 16	0.01	0.40±0.02	0.40±0.03	2.93	24	6.7±0.5	9.0±0.6	0
SMM104	18 20.0 37.9	-16 02 56	0.12	0.29±0.01	0.63±0.07	2.87	22	10±1	16±2	0
SMM105	18 20.0 37.9	-16 06 22	0.07	0.20±0.01	0.23±0.02	2.28	13	3.9±0.3	14±1	0
SMM106	18 20.0 38.0	-16 01 34	0.18	1.16±0.05	3.0±0.4	2.82	21	50±7	80±10	0
SMM107	18 20.0 38.0	-16 03 20	0.05	0.21±0.01	0.22±0.02	2.85	22	3.7±0.3	5.8±0.4	0
SMM108	18 20.0 38.1	-15 59 16	0.16	0.99±0.04	2.4±0.3	2.72	18	40±5	80±10	1
SMM109	18 20.0 38.5	-15 58 08	0.13	0.58±0.02	1.1±0.1	2.74	19	19±2	36±4	0
SMM110[e]	18 20.0 38.7	-16 09 04	0.14	0.26±0.01	0.5±0.1	$\cdots$	$\cdots$	9±2	$\cdots$	0
SMM111	18 20.0 39.0	-16 07 52	0.19	0.40±0.02	1.6±0.2	1.99	11	27±4	140±20	0
SMM112	18 20.0 39.1	-16 06 00	0.16	0.55±0.02	1.8±0.2	2.60	16	30±4	71±9	1
SMM113	18 20.0 39.5	-16 06 52	0.10	0.43±0.02	0.74±0.08	3.06	30	12±1	12±1	0
SMM114	18 20.0 39.7	-16 02 16	0.14	0.47±0.02	1.5±0.2	1.80	10	25±3	160±20	1
SMM115[e]	18 20.0 39.7	-16 09 22	0.10	0.26±0.01	0.38±0.06	$\cdots$	$\cdots$	6.2±0.9	$\cdots$	0
SMM116	18 20.0 40.6	-16 07 04	0.08	0.30±0.01	0.35±0.03	2.90	23	5.9±0.5	8.3±0.6	0
SMM117	18 20.0 41.2	-16 02 22	0.12	0.21±0.01	0.40±0.04	$\cdots$	$\cdots$	6.6±0.7	$\cdots$	0
SMM118[e]	18 20.0 41.6	-16 08 26	0.12	0.59±0.02	1.1±0.2	2.64	17	19±3	43±6	0
SMM119	18 20.0 42.0	-16 07 22	0.11	0.40±0.02	0.59±0.06	2.10	11	10±1	45±4	0
SMM120	18 20.0 42.7	-16 01 36	0.03	0.16±0.01	0.10±0.01	$\cdots$	$\cdots$	1.64±0.09	$\cdots$	0
SMM121[e]	18 20.0 42.9	-16 08 26	0.19	0.59±0.02	1.8±0.3	2.82	21	30±5	50±7	1

[a]The uncertainties stated in this table are composed of the uncertainties in the gain calibration, the sky opacities, and the corrections due to the error beam. These uncertainties are typically significantly larger than the random measurement errors associated with the rms flux of the map. The exception is the peak flux, where the random error of $\sigma = 0.027$ Jy beam^{-1} dominates the systematic error for the clumps with lower peak fluxes.

[b]The systematic uncertainty in the spectral index, α, is 13%. These systematic uncertainties, which are composed of the uncertainties in the gain calibration and sky opacities, dominate the random errors on the spectral index.

[c]See Section 3.2 for a discussion of the uncertainties in the temperatures. Temperatures are omitted where high spectral index makes them incalculable, or where no reliable spectral index can be calculated (see text). All of the temperatures above 40 K should be considered highly uncertain, indicating only that a clump is probably hot.

[d]Number of MSX point sources contained within the clump's $0.5S_{\mathrm{peak}}$ contour.

[e]Denotes a clump to which corrections for free-free emission have been applied in the calculation of the spectral index, dust temperature, and masses. The free-free correction has *not* been applied to the peak and integrated fluxes listed here.

Table 2.   Properties of the 450 μm Clumps

Name[a] (M17-)	R.A. (J2000)	Dec. (J2000)	$R_{\rm eff}$ (pc)	$S_{\rm peak}$[b] Jy beam^{-1}	$S_{450}^{\rm int}$[b] (Jy)	$M_{{\rm T}_d=30K}$[b] ($M_\odot$)	$n_{\rm psc}$[c]
SMM4A	18 20.0 03.0	-16 00 46	0.06	1.5±0.2	2.4±0.3	4.2±0.6	0
SMM7B	18 20.0 03.6	-16 02 22	0.07	1.6±0.2	2.6±0.4	4.5±0.7	0
SMM7A	18 20.0 04.9	-16 02 24	0.09	2.4±0.3	5.6±0.9	10±2	0
SMM8A	18 20.0 05.4	-16 01 30	0.09	3.7±0.4	8±1	13±2	0
SMM9B	18 20.0 05.9	-16 04 44	0.11	3.4±0.4	11±2	19±3	0
SMM11B	18 20.0 06.1	-16 01 52	0.11	3.3±0.4	8±1	14±3	0
SMM10A	18 20.0 06.1	-16 04 22	0.09	2.9±0.3	7±1	13±2	0
SMM15A	18 20.0 06.7	-16 05 54	0.06	1.3±0.2	2.0±0.3	3.4±0.5	0
SMM9A	18 20.0 07.4	-16 04 52	0.09	2.4±0.3	6±1	10±2	0
SMM11A	18 20.0 07.6	-16 02 30	0.07	1.8±0.2	2.9±0.4	5.1±0.8	0
SMM18A	18 20.0 09.0	-16 03 50	0.06	1.3±0.2	2.4±0.3	4.2±0.6	0
SMM18B	18 20.0 09.1	-16 03 24	0.15	2.7±0.3	13±2	22±4	0
SMM17A	18 20.0 09.2	-16 04 18	0.05	1.6±0.2	1.9±0.3	3.3±0.5	0
SMM18C	18 20.0 09.4	-16 02 44	0.06	1.8±0.2	2.8±0.4	4.8±0.7	0
SMM20B	18 20.0 09.5	-16 01 22	0.07	2.2±0.3	2.8±0.4	4.9±0.7	0
SMM23B	18 20.0 10.1	-16 07 08	0.11	4.2±0.5	12±2	21±4	0
SMM22A	18 20.0 10.5	-15 58 48	0.04	1.9±0.2	1.7±0.2	3.0±0.4	0
SMM21B	18 20.0 10.5	-16 02 34	0.05	1.4±0.2	2.0±0.3	3.5±0.5	0
SMM20A	18 20.0 10.6	-16 02 02	0.11	1.8±0.2	7±1	11±2	0
SMM24A	18 20.0 10.9	-16 06 30	0.11	2.4±0.3	7±1	12±2	0
SMM21A	18 20.0 10.9	-16 02 48	0.07	1.3±0.2	2.6±0.4	4.6±0.6	0
SMM21C	18 20.0 11.2	-16 02 24	0.05	1.4±0.2	1.7±0.2	3.0±0.4	0
SMM23A	18 20.0 11.5	-16 07 08	0.12	4.9±0.6	13±3	23±4	0
SMM27A	18 20.0 13.0	-16 00 28	0.07	2.0±0.2	4.0±0.6	7±1	0
SMM28A	18 20.0 13.1	-16 04 46	0.08	1.9±0.2	3.4±0.5	5.8±0.9	0
SMM29A	18 20.0 13.3	-16 05 02	0.06	1.5±0.2	2.6±0.4	4.5±0.6	0
SMM30A	18 20.0 14.4	-16 06 12	0.11	3.0±0.4	10±2	17±3	0
SMM30B	18 20.0 14.4	-16 05 56	0.07	2.9±0.3	5.4±0.8	9±1	0
SMM31A	18 20.0 14.5	-16 07 00	0.16	5.9±0.7	29±6	50±10	0
SMM32A	18 20.0 14.8	-16 07 56	0.17	13±2	50±10	90±20	0
SMM37B	18 20.0 14.8	-16 05 30	0.10	3.0±0.4	9±2	15±3	0
SMM33A	18 20.0 15.4	-16 07 34	0.12	6.4±0.8	23±4	40±8	0
SMM34A	18 20.0 15.4	-16 04 48	0.06	2.0±0.2	2.8±0.4	4.9±0.7	0
SMM35A	18 20.0 15.5	-16 09 28	0.14	5.4±0.6	23±5	40±8	0
SMM36A	18 20.0 16.0	-16 08 54	0.18	17±2	70±10	120±30	0
SMM37A	18 20.0 16.2	-16 05 50	0.11	5.1±0.6	14±2	24±4	0
SMM33B	18 20.0 16.5	-16 07 26	0.08	4.0±0.5	7±1	13±2	0
SMM41A	18 20.0 16.9	-16 05 30	0.09	2.3±0.3	5.8±0.8	10±1	0
SMM45A	18 20.0 16.9	-16 06 28	0.06	1.6±0.2	2.4±0.3	4.2±0.6	0
SMM43A	18 20.0 17.6	-16 08 32	0.03	1.9±0.2	1.8±0.2	3.1±0.4	0
SMM44A	18 20.0 18.1	-16 04 24	0.06	2.4±0.3	3.9±0.6	7±1	0
SMM45B	18 20.0 18.7	-16 06 08	0.06	2.0±0.2	2.9±0.4	5.0±0.7	0
SMM46A	18 20.0 19.4	-16 09 44	0.14	10±1	27±5	46±9	0
SMM48A	18 20.0 21.9	-16 06 12	0.10	2.0±0.2	6±1	10±2	1
SMM49A	18 20.0 23.0	-15 58 38	0.10	1.6±0.2	5.7±0.8	10±1	0

Table 2—Continued

Name[a] (M17-)	R.A. (J2000)	Dec. (J2000)	R_{eff} (pc)	S_{peak}[b] Jy beam^{-1}	S_{450}^{int} [b] (Jy)	$M_{\mathrm{T}_d=30K}$[b] ($M_\odot$)	n_{psc}[c]
SMM51A	18 20.0 24.1	-15 59 06	0.12	2.0±0.2	8±2	14±3	0
SMM52A	18 20.0 25.1	-16 03 50	0.07	3.7±0.4	7±1	13±2	0
SMM54A	18 20.0 25.1	-16 06 20	0.12	3.6±0.4	11±2	19±4	0
SMM55A	18 20.0 25.1	-16 05 28	0.12	2.8±0.3	10±2	18±3	0
SMM61A	18 20.0 25.5	-16 07 36	0.07	1.5±0.2	3.1±0.5	5.3±0.8	0
SMM56A	18 20.0 25.8	-16 05 58	0.14	2.7±0.3	14±2	24±4	0
SMM60A	18 20.0 25.8	-16 02 04	0.08	1.9±0.2	3.9±0.6	7±1	0
SMM57A	18 20.0 25.8	-16 02 22	0.07	1.7±0.2	3.2±0.4	5.6±0.7	0
SMM62A	18 20.0 26.6	-16 01 46	0.07	1.7±0.2	3.0±0.5	5.2±0.8	0
SMM65A	18 20.0 27.2	-16 07 12	0.03	1.9±0.2	1.5±0.2	2.5±0.3	0
SMM64A	18 20.0 27.3	-16 08 28	0.08	5.3±0.6	7±1	13±2	0
SMM67A	18 20.0 28.1	-16 00 30	0.09	1.9±0.2	5.0±0.8	9±1	0
SMM70A	18 20.0 28.7	-16 01 24	0.15	4.1±0.5	18±4	32±6	0
SMM68A	18 20.0 29.0	-16 08 56	0.02	1.7±0.2	1.1±0.1	1.8±0.2	0
SMM71A	18 20.0 29.5	-16 07 32	0.14	1.8±0.2	10±2	18±3	0
SMM73A	18 20.0 29.7	-16 02 06	0.14	5.7±0.7	23±4	39±8	1
SMM80A	18 20.0 29.8	-16 02 40	0.10	3.4±0.4	9±1	16±2	0
SMM77A	18 20.0 30.8	-16 08 46	0.09	6.8±0.8	16±3	28±5	0
SMM81B	18 20.0 31.0	-16 08 18	0.13	4.6±0.5	17±3	29±6	0
SMM80B	18 20.0 31.5	-16 02 16	0.10	3.9±0.5	9±2	16±3	0
SMM82A	18 20.0 32.2	-16 01 02	0.15	3.3±0.4	18±4	31±6	0
SMM81A	18 20.0 32.4	-16 08 28	0.12	5.0±0.6	14±3	24±4	0
SMM87A	18 20.0 32.6	-15 59 00	0.14	4.2±0.5	19±4	33±7	0
SMM85A	18 20.0 32.6	-16 02 50	0.06	1.6±0.2	3.1±0.4	5.3±0.7	0
SMM86A	18 20.0 32.7	-16 01 48	0.19	25±3	90±20	160±40	1
SMM88A	18 20.0 32.9	-16 04 12	0.13	4.7±0.6	14±3	24±5	0
SMM93A	18 20.0 33.0	-16 07 44	0.19	2.4±0.3	18±4	30±6	0
SMM88B	18 20.0 33.0	-16 03 44	0.07	2.0±0.2	4.1±0.6	7±1	0
SMM91A	18 20.0 33.7	-15 58 10	0.15	2.9±0.4	15±3	25±4	0
SMM92B	18 20.0 33.8	-15 59 52	0.15	4.8±0.6	23±5	39±8	0
SMM92A	18 20.0 34.1	-16 00 18	0.14	3.2±0.4	15±3	26±5	0
SMM94A	18 20.0 34.2	-15 58 38	0.11	3.4±0.4	11±2	18±3	0
SMM97C	18 20.0 34.7	-16 00 36	0.11	4.7±0.6	20±3	34±6	0
SMM96B	18 20.0 34.8	-16 04 34	0.13	3.9±0.5	15±3	27±5	0
SMM95A	18 20.0 35.1	-16 08 32	0.16	6.2±0.7	25±5	44±9	0
SMM98A	18 20.0 35.2	-16 06 06	0.15	9±1	34±7	60±10	0
SMM96A	18 20.0 35.2	-16 04 58	0.14	4.1±0.5	17±3	29±6	0
SMM97A	18 20.0 35.4	-16 00 44	0.13	5.4±0.6	21±4	37±7	1
SMM98C	18 20.0 35.8	-16 05 32	0.12	3.3±0.4	13±2	22±4	0
SMM97B	18 20.0 36.7	-16 00 36	0.11	3.5±0.4	11±2	19±3	0
SMM98B	18 20.0 36.7	-16 05 54	0.11	2.8±0.3	9±2	16±3	0
SMM100A	18 20.0 36.9	-15 59 46	0.17	3.2±0.4	20±4	34±6	0
SMM99A	18 20.0 37.0	-15 58 02	0.06	2.9±0.3	4.3±0.7	7±1	0
SMM101A	18 20.0 37.6	-16 01 54	0.07	4.2±0.5	7±1	11±2	0
SMM102A	18 20.0 37.6	-15 57 38	0.12	2.3±0.3	8±1	13±3	0

Table 2—Continued

Name[a] (M17-)	R.A. (J2000)	Dec. (J2000)	R_{eff} (pc)	S_{peak}[b] Jy beam^{-1}	S_{450}^{int}[b] (Jy)	$M_{T_d=30K}$[b] ($M_\odot$)	n_{psc}[c]
SMM104A	18 20.0 37.7	-16 02 52	0.06	1.7±0.2	2.5±0.4	4.3±0.6	0
SMM108A	18 20.0 38.1	-15 59 12	0.14	5.2±0.6	19±3	32±6	0
SMM106A	18 20.0 38.1	-16 01 36	0.14	5.2±0.6	17±3	30±6	0
SMM109A	18 20.0 38.3	-15 58 06	0.09	3.1±0.4	7±1	11±2	0
SMM104B	18 20.0 38.5	-16 02 40	0.05	1.4±0.2	1.9±0.2	3.2±0.4	0
SMM95B	18 20.0 38.7	-16 08 14	0.08	1.6±0.2	4.0±0.6	7±1	0
SMM112A	18 20.0 39.4	-16 05 58	0.10	2.0±0.2	6±1	11±2	0
SMM113A	18 20.0 39.7	-16 06 58	0.11	1.8±0.2	7±1	12±2	0
SMM118A	18 20.0 41.5	-16 08 28	0.07	2.3±0.3	4.6±0.7	8±1	0
SMM121A	18 20.0 42.3	-16 08 40	0.04	2.1±0.2	2.3±0.3	4.0±0.5	0
SMM121B	18 20.0 43.0	-16 08 24	0.10	3.1±0.4	8±1	14±3	1

[a]The names of the 450 μm clumps have been set to reflect the names of the 850 μmclumps in which their peaks appear. Thus, clumps SMM 21A–21C are the three 450 μm clumps whose peaks appear within the boundaries of 850 μm clump SMM 21.

[b]The uncertainties stated in this table are composed of the uncertainties in the gain calibration, the sky opacities, and the corrections due to the error beam. These uncertainties are typically significantly larger than the random errors associated with the rms flux of the map. The exception is the peak flux, where the random error of $\sigma = 0.32$ Jy beam^{-1} dominates the systematic error for the clumps with lower peak fluxes.

[c]Number of MSX point sources contained within the clump's $0.5S_{\text{peak}}$ contour.

Table 3.　Mass Function Parameters of Best Fit

Fit Type	Waveband (μm)	A_0	A_1	M_{peak}[c] ($M_\odot$)	$\langle M \rangle$[c] ($M_\odot$)	M_{break} ($M_\odot$)	α_{low}	α_{high}
N($>M$)[a]	850	2.5 ± 0.1	1.06 ± 0.07	3.9 ± 0.5	21 ± 2	17^{+19}_{-3}	$-1.35^{+0.03}_{-0.11}$	$-2.7^{+0.2}_{-1.0}$
$\Delta N/\Delta M$[b]	850	2.6 ± 0.1	1.3 ± 0.1	2.5 ± 0.5	32 ± 3	8 ± 2	-0.01 ± 0.26	-1.5 ± 0.1
N($>M$)[a]	450	2.54 ± 0.07	0.87 ± 0.09	5.7 ± 0.6	19 ± 1	18 ± 4	-1.5 ± 0.2	-3.1 ± 0.4
$\Delta N/\Delta M$[b]	450	2.7 ± 0.1	1.2 ± 0.1	3 ± 1	30 ± 5	19 ± 6	-0.5 ± 0.2	-1.9 ± 0.3

[a]Uncertainties on fits to the CMFs correspond to the 95% confidence interval on either side of the most likely value of the fitted parameter, as determined from 10^5 Monte Carlo simulations of the data. The unequal upper and lower uncertainty bounds on the fit to the 850 μm CMF reflect the skew of the distribution of the fitted parameters.

[b]Uncertainties on fits to the DMFs were calculated using a standard nonlinear least-squares fit to the binned data. The stated uncertainties are 2 σ uncertainties, to match the 95% confidence interval used for the CMF uncertainties.

[c]The mean mass, $\langle M \rangle$, and peak mass, M_{peak} of the lognormal distribution are not parameters of the fit; they are calculated from A_0 and A_1 using the transformation equations $\langle M \rangle = \exp(A_0 + \frac{1}{2}A_1^2)$ and $M_{\mathrm{peak}} = \exp(A_0 - A_1^2)$.